Published for SISSA by Springer

Received: *February 22, 2023*
Revised: *July 20, 2023*
Accepted: *July 31, 2023*
Published: *August 17, 2023*

Methods and restrictions to increase the volume of resonant rectangular-section haloscopes for detecting dark matter axions

J.M. García-Barceló,[a,1] **A. Álvarez Melcón,**[a] **A. Díaz-Morcillo,**[a] **B. Gimeno,**[b] **A.J. Lozano-Guerrero,**[a] **J. Monzó-Cabrera,**[a] **J.R. Navarro-Madrid**[a] **and P. Navarro**[a]

[a] *Departamento de Tecnologías de la Información y las Comunicaciones, Universidad Politécnica de Cartagena, Plaza del Hospital 1, 30302 Cartagena, Spain*

[b] *Instituto de Física Corpuscular (IFIC), CSIC-University of Valencia, 46980 – Valencia, Spain*

E-mail: josemaria.garcia@upct.es, alejandro.alvarez@upct.es, alejandro.diaz@upct.es, benito.gimeno@uv.es, antonio.lozano@upct.es, juan.monzo@upct.es, joser.navarro@upct.es, pablonm.ct.94@gmail.com

Abstract: Haloscopes are resonant cavities that serve as detectors of dark matter axions when they are immersed in a strong static magnetic field. In order to increase the volume and improve space compatibility with dipole or solenoid magnets for axion searches, various haloscope design techniques for rectangular geometries are discussed in this study. The volume limits of two types of haloscopes are explored: those based on single cavities and those based on multicavities. In both cases, possibilities for increasing the volume of long and/or tall structures are presented. For multicavities, 1D geometries are explored to optimise the space in the magnets. Also, 2D and 3D geometries are introduced as a first step in laying the foundations for the development of these kinds of topologies. The results prove the usefulness of the developed methods, evidencing the ample room for improvement in rectangular haloscope designs nowadays. A factor of three orders of magnitude improvement in volume compared with a single cavity based on the WR-90 standard waveguide is obtained with the design of a long and tall single cavity. Similar procedures have been applied for long and tall multicavities. Experimental measurements are shown for prototypes based on tall multicavities and 2D structures, demonstrating the feasibility of using these types of geometries to increase the volume of real haloscopes.

Keywords: Axions and ALPs, Particle Nature of Dark Matter

ArXiv ePrint: 2302.10569

[1] Corresponding author.

https://doi.org/10.1007/JHEP08(2023)098

JHEP08(2023)098

Contents

1 Introduction

Research in the field of axions and other particles that conform to the Standard Model and potentially contribute to the enigma of dark matter has attracted significant attention in recent decades [1, 2]. Axions, initially proposed by Weinberg [3] and Wilczek [4], offer a potential resolution to the longstanding Charge Conjugation-Parity (CP) problem [1, 2]. Subsequently, the notion of axions as dark matter candidates gained attention through the concept of misalignment [5–7].

Over the past thirty years, numerous research groups have dedicated their efforts to developing experimental systems for detecting dark matter axions [8]. These experiments rely on the inverse Primakoff effect [9]. Depending on the source of axions, detection techniques can be classified into three categories: Light Shining through Walls (LSW), helioscopes, and haloscopes. LSW experiments artificially generate axion particles, while helioscopes and haloscopes exploit external natural sources, namely the sun and the galactic halo, respectively. In all cases, axion-to-photon conversion is facilitated by a strong static magnetic field. Haloscopes, in particular, employ high-quality factor resonators, such as microwave cavities, to enhance this conversion process [10].

The most competitive axion detection experiments currently encompass the haloscope scenario, with the ADMX (Axion Dark Matter eXperiment) [11] and CAPP (Center for

JHEP08(2023)098

Axion and Precision Physics) [12] projects leading the field at frequencies below and above 1 GHz, respectively. For helioscopes, the CAST (CERN Axion Solar Telescope) experiment [13], now decommissioned, and the future IAXO (International Axion Observatory) [14] play significant roles. The BabyIAXO magnet prototype is being developed as a precursor to IAXO, providing a platform for both helioscope and haloscope axion observations [15]. The large-volume magnets in IAXO and BabyIAXO offer a good cost-effectiveness relationship and enable the implementation of large haloscopes operating at X-band frequencies. These experiments strive to achieve sensitivities aligned with the KSVZ (Kim-Shifman-Vainshtein-Zakharov) and DFSZ (Dine-Fischler-Srednicki-Zhitnitsky) models, which postulate a higher probability of detecting axions. The ADMX experiment has successfully reached these sensitivities in the ultra-high frequency (UHF) range [16]. Notably, the CAPP (Center for Axion and Precision Physics Research) group recently outlined an axion dark matter search experiment employing a haloscope with DFSZ sensitivity across the 4.51 to 4.59 μeV axion mass range [12]. Additionally, the HAYSTAC (Haloscope At Yale Sensitive To Axion Cold Dark Matter) team has reported KSVZ sensitivity results from two independent searches for dark matter axions across 16.96 to 17.28 μeV and 23.15 to 24.0 μeV axion mass ranges [17, 18]. These collaborations are making substantial progress towards achieving theoretically significant sensitivities in haloscopes. Other experimental groups, such as RADES [19], QUAX [20], and KLASH [21], have also demonstrated notable advancements in haloscope utilization in recent years.

The complete axion detection system comprises several key components. First, due to the extremely weak axion-photon coupling, a cryogenic environment with temperatures in the Kelvin range is necessary to minimize thermal noise levels. Second, the received radio frequency (RF) power within the haloscope is amplified, filtered, down-converted, and subsequently detected by a low-noise coupled receiver. Finally, the receiver performs analog-to-digital conversion and utilizes Fast Fourier Transform algorithms for data post-processing [19].

A major goal of an axion detection system is to enhance the axion-photon conversion sensitivity of the haloscope, which for a given signal-to-noise ratio ($\frac{S}{N}$) can be obtained as [22][1]

$$g_{a\gamma} = \left(\frac{\frac{S}{N} k_B T_{\text{sys}} (1+\beta)^2}{\rho_a C V \beta Q_0} \right)^{\frac{1}{2}} \frac{1}{B_e} \left(\frac{m_a^3}{Q_a \Delta t} \right)^{\frac{1}{4}} \tag{1.1}$$

where k_B is the Boltzmann constant, T_{sys} is the noise temperature of the system, β is the extraction coupling factor (with $\beta = 1$ for a critical coupling operation regime to achieve the maximum power transfer), ρ_a is the dark matter density, C is the form or geometric factor, V is the haloscope or cavity volume, Q_0 is the unloaded quality factor, B_e is the peak magnitude of the static external magnetic field $\vec{B}_e$, m_a is the axion mass (proportional to the working frequency of the experiment), Q_a is the axion quality factor, and Δt is the

[1]The fact that this equation only applies to one frequency point must be noted. For the search for axions utilizing the frequency sweep with a tuning system, the scanning rate parameter $\frac{dm_a}{dt}$ must be optimized. The figure of merit in the first criterion is contingent upon the factor QVC, whereas in the second criterion, it relies on QV^2C^2. A detailed analysis of the scanning rate can be found in [23]. This work acknowledges the validity of equation (1.1)'s optimization for the sake of simplicity.

JHEP08(2023)098

time window used in the data taking. Here Q_0 is assumed to be much lower than the axion quality factor ($Q_a \approx 10^6$) [23]. It should be emphasized that the external static magnetic field ($\vec{B}_e$) depends on the type of magnet employed in the experiment (dipole or solenoid), and its spatial distribution and polarisation must be considered in order to boost the axion-photon conversion.

The form factor provides the coupling between $\vec{B}_e$ and the radio frequency electric field ($\vec{E}$) induced into the cavity by the axion-photon interaction. It can be written as:

$$C = \frac{|\int_V \vec{E} \cdot \vec{B}_e \, dV|^2}{\int_V |\vec{B}_e|^2 \, dV \int_V \varepsilon_r |\vec{E}|^2 \, dV} \tag{1.2}$$

where ε_r is the relative electric permittivity filling the cavity medium (generally air or vacuum). Therefore, the factors that can be adjusted and optimised in the design of a haloscope resonator are β, C, V, and Q_0.

The resonant frequency of a rectangular cavity for TE_{mnp} and TM_{mnp} modes is given by

$$f_{mnp} = \frac{c}{2\sqrt{\mu_r \varepsilon_r}} \sqrt{\left(\frac{m}{a}\right)^2 + \left(\frac{n}{b}\right)^2 + \left(\frac{p}{d}\right)^2} \tag{1.3}$$

where c is the speed of light in vacuum, μ_r is the relative magnetic permeability of the medium inside the cavity ($\mu_r = \varepsilon_r = 1$ is assumed in this work), m, n, and p are integers that denote the number of maxima of the electric field along the x, y, and z axes, respectively, and a, b, and d are the width, height, and length of the cavity, respectively. For TE_{mnp} modes, the allowed indexes are: $m = 0, 1, 2, \ldots$; $n = 0, 1, 2, \ldots$; $p = 1, 2, 3, \ldots$, although m and n can not be zero simultaneously. For TM_{mnp} modes: $m = 1, 2, 3, \ldots$; $n = 1, 2, 3, \ldots$ and $p = 0, 1, 2, \ldots$. As it is indicated by this equation, resonant frequencies are dependent on the three cavity dimensions. This relationship actually suggests difficulties in increasing volume and frequency at the same time without increasing mode clustering.

The magnets commonly employed in experiments dedicated to the detection of dark matter axions predominantly consist of solenoids (see figure 1a). These solenoidal magnets find application in research initiatives such as ADMX [16], CAPP [12], and HAYSTAC [24]. The axial magnetic field they generate (along the z-axis) aligns favorably with the cylindrical shape of the cavity, facilitating the alignment of the electric field of the TM_{010} cylindrical mode with the external magnetic field. This alignment ensures an optimal form factor. In contrast, powerful accelerator dipole magnets (see figure 1b), such as the one employed in the CAST experiment, produce a high transverse magnetic field. Consequently, a rectangular cavity with a TE_{101} mode is employed, resulting in vertical polarization and the electric field being predominantly parallel to the dipole's static magnetic field [22, 25]. Another noteworthy example is BabyIAXO, a superconducting toroidal magnet, for which the magnetic field pattern can be consulted in [15]. For the sake of simplicity, it can be considered a dipole magnet in this context. Table 1 provides a description of the most commonly used or planned magnets employed by various research groups in the near term. Figure 1 illustrates the optimal orientation of rectangular and cylindrical cavities for dipole

JHEP08(2023)098

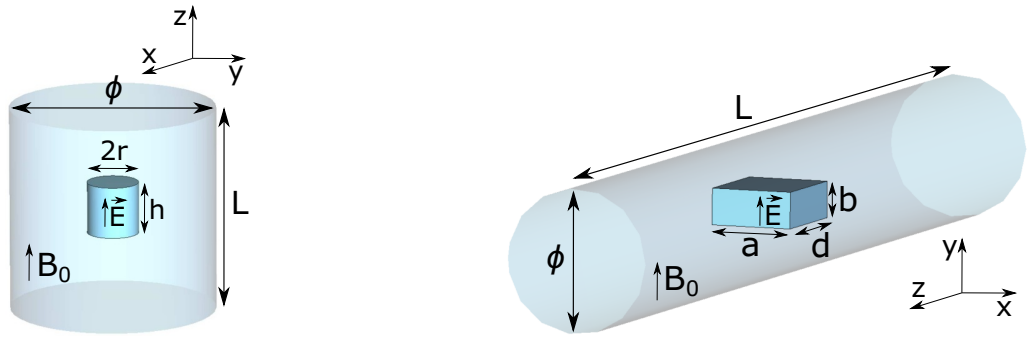

(a) (b)

Figure 1. Examples of (a) a solenoid magnet bore with a cylindrical cavity of radius r and height h operating with the TM_{010} cylindrical mode and (b) a dipole magnet bore with a rectangular cavity of width a, height b, and length d working with the TE_{101} rectangular mode. The direction of the magnetic field is mostly in the z-axis for the solenoid magnet and in the y-axis for the dipole magnet. Light blue objects represent solenoid and dipole magnets, while darker blue objects represent microwave cavities. Although it is not presented in this figure, it is assumed that the probes for the external couplings will be positioned at the upper wall of the cavities (z-axis in (a) and y-axis in (b)).

Magnet	Type	B_e (T)	T_p (K)	ϕ (mm)	L_{bore} (m)	$\frac{B_e^2 V}{T_p}$ $(\frac{T^2 m^3}{K})$	References
BabyIAXO	Quasi-dipole	~ 2.5	4.2	600	10	4.207	[15]
CAST	Dipole	9	1.8	42.5	9.25	0.591	[26]
SM18	Dipole	11	4.2	54	2	0.132	[27]
MRI (ADMX-EFR)	Solenoid	~ 9	0.1	800	0.513	215.03	[28, 29]
Wang NMR (ADMX-1G)	Solenoid	8	0.1	600	1.1	199.05	[30, 31]
Oxford Instr. (CAPP-12TB)	Solenoid	~ 12	0.025	320	0.4	185.3	[12, 32]
Cryomagnetics (ADMX-HF)	Solenoid	9	0.025	175	0.4	31.17	[30, 33]
AMI (CAPP-8TB)	Solenoid	8	0.05	165.4	0.476	13.1	[34]
BlueFors (ORGAN)	Solenoid	14	0.03	65	0.445	9.633	[35, 36]
Cryomagnetics (HAYSTAC)	Solenoid	9	0.127	140	0.56	5.496	[24]
18T HTS (CAPP)	Solenoid	~ 18	0.11	70	0.467	5.294	[37, 38]
Canfranc	Solenoid	10	0.1	150	0.2	3.53	[39, 40]
QUAX	Solenoid	~ 1	0.12	150	0.5	0.075	[41]

Table 1. Characteristics of different magnets for axion data taking. ϕ and L_{bore} are the diameter and length, respectively, of the magnets. A figure of merit for the magnet ($\frac{B_e^2 V}{T_p}$) is included in this table according to equation (1.1), which assumes a haloscope filling the whole volume of the magnet. In this case, T_p represents the physical temperature of the bore region in which the cavity is immersed.

and solenoid magnets, respectively. In this study, a constant magnetic field $\vec{B}_e = B_e\,\hat{y}$ in the dipole and quasi-dipole [15] magnets has been adopted as an approximation for calculating the form factor.

In general, the aspect ratio of dipole magnet bores tends to have a significantly greater length compared to their diameter. Conversely, the length and diameter of solenoid magnet

JHEP08(2023)098

bores exhibit closer similarity. Consequently, the primary objective for enhancing volume entails adjusting the haloscope geometry to occupy as much of the available space within the bore. One early endeavor to capitalize on long cavities involved the design, development, and implementation of a toroidal-shaped cavity by the CAPP group [42, 43], with the BabyIAXO magnet presenting an ideal candidate for this purpose. However, it is worth noting that the utilization of novel topologies, such as tall structures in rectangular geometries, holds promise as a compelling concept [42, 43].

The primary aim of this study is to analyze the potential for augmenting the volume of a haloscope that employs rectangular cavities, thereby effectively improving the sensitivity for axion detection. Subsequent exploration of cylindrical cavities is envisioned for future investigations. The maximum volume allowable in a haloscope design primarily hinges on four key factors: the cavity shape, the operating electromagnetic mode and frequency, the use of multicavity concepts, and the geometry and type of magnet (and consequently, the direction of the magnetic field) employed for the axion measurement campaign.

Section 2 delineates the investigations conducted in this study to ascertain the volume limits of haloscopes based on individual rectangular cavities. Three distinct cavity types have been examined: long, tall, and large (long and tall). In determining these limits, careful consideration has been given to the frequency separation between resonant modes, known as mode clustering. This phenomenon can have a detrimental impact on the form factor (C), which, as previously mentioned, is an essential parameter alongside volume and quality factor in enhancing axion detection performance. By comparing high-volume structures within the prescribed dimension limits for each case against a standard single cavity, the considerable potential of these prototypes has been demonstrated. Additionally, the quality factor of each case has been taken into account for these comparisons.

Subsequently, section 3 addresses the exploration of extended concepts of long, tall, and large structures within the realm of 1D multicavities. This technique involves the direct coupling of subcavities through iris windows. The foundations for designing such haloscopes are explained, followed by an examination of multicavities with mode clustering as the number of subcavities increases. Three distinct cases are considered: all-inductive, all-capacitive, and alternated (inductive/capacitive) irises. The figure of merit, encompassing the form factor, quality factor, and volume, is then scrutinized for 1D multicavities by increasing the lengths, heights, and both lengths and heights (large type) of the subcavities. In each of these three cases, the potential for coupling subcavities in three possible directions-length, height, and width (corresponding to the dipole magnet's z-axis, y-axis, and z-axis, respectively, as illustrated in figure 1b) is showcased. These haloscope structures are evaluated in relation to both dipole and solenoid magnets, taking into account the magnets listed in table 1. A comparison is made between these structures and standard single cavities to underscore their capacity for enhancing the figure of merit. Furthermore, experimental measurement results of a fabricated structure for the case of a 1D multicavity with high subcavities coupled in length using all-inductive irises are presented as a proof of concept.

Section 4 lays out the foundations for extending the multicavity concept to 2D and 3D structures, involving the application of couplings between subcavities in two and three directions, respectively. Various examples of 2D and 3D multicavity topologies are pre-

JHEP08(2023)098

sented, highlighting their advantages over 1D structures for optimizing the utilization of magnets in axion searches. For the 2D case, a prototype has been designed, manufactured, and measured, serving as a validation of the explored concepts.

Lastly, in section 5, the conclusions and future prospects stemming from this work are examined.

2 Single cavities

For rectangular cavities working in dipole magnets, the TE_{101} mode is selected since it is the one that maximises the form factor described in equation (1.2). For this mode, the height of the cavity b does not affect the resonant frequency, so it can be increased as desired in order to increase the cavity volume. However, there is a limit where the cavity height cannot be increased due to the proximity of the higher order modes with $n \neq 0$ (the closest mode will be the TE_{111}/TM_{111} in this case). This situation may hinder the correct identification of the mode and can even reduce the form factor in some cases.

Also, studying equation (1.3), it is observed that the best option to increase the length of the haloscope without decreasing the resonant frequency is by reducing slightly the width for the TE_{101} mode. This reduction is small compared to the length gained, so the total volume will increase. Additionally, when the length of the cavity is much larger than its width, the resonant frequency becomes almost independent of the cavity length $f_{TE_{101}} \approx \frac{c}{2a}$. Here, again, the length limit is imposed by the proximity of the next resonant mode (mode clustering with the TE_{102} in this case).

2.1 Long cavities

The limitation on increasing the length d of a rectangular single cavity is based on the mode separation between the modes TE_{101} and TE_{102}. Figure 2a plots the relative mode separation ($\Delta f = \frac{|f_{\text{axion}} - f_{\text{neighbour}}|}{|f_{\text{axion}}|} \times 100\%$, where f_{axion} is the resonant frequency of the mode induced by the axion-photon conversion and $f_{\text{neighbour}}$ is the resonant frequency of the closest mode) for a rectangular cavity as a function of d/a, which is valid for any resonant frequency of TE_{101} and relatively small ($\sim a$) height b. The results show a rapid decrease in the mode separation when d/a increases. If the next mode is far enough away in frequency, the form factor will be the theoretical maximum value for any cavity size: $C_{TE_{101}} = 64/\pi^4 = 0.657$, obtained from equation (1.2).

The unloaded quality factor of a TE_{10p} mode in a rectangular waveguide cavity resonator without dielectric losses can be expressed as [44]

$$Q_0 = \frac{1}{2}\sqrt{\frac{\pi\,\sigma}{\varepsilon_0\, f_{10p}}}\,\frac{b\left(a^2+d^2\right)^{3/2}}{ad\left(a^2+d^2\right)+2b\left(a^3+d^3\right)} \tag{2.1}$$

where σ is the electrical conductivity of the cavity walls ($\sigma = 2\times10^9\,\mathrm{S/m}$ is assumed, which corresponds with copper at cryogenic temperatures), $\varepsilon_0 \approx 8.854\times10^{-12}\,\mathrm{F/m}$ is the vacuum electric permittivity, and f_{10p} is the resonant frequency of a TE_{10p} mode. Plotting this equation (see figure 2b), it can be observed that the unloaded quality factor decreases for

JHEP08(2023)098

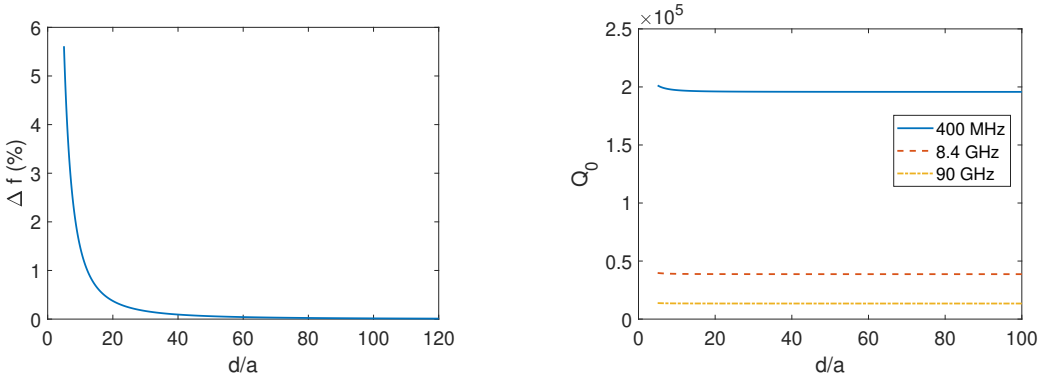

(a) (b)

Figure 2. (a) Relative mode separation between modes TE_{101} and TE_{102} of a long rectangular cavity as a function of d/a for any frequency and (b) Q_0 of the TE_{101} mode as a function of d/a for three frequencies (0.4, 8.4, and 90 GHz).

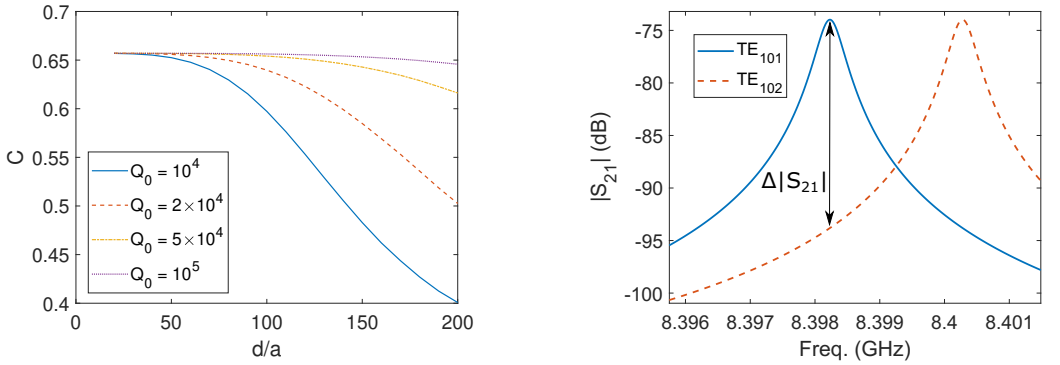

(a) (b)

Figure 3. (a) Form factor versus d/a for several Q_0 values, and (b) example of two close resonances with an amplitude difference of $\Delta|S_{21}| = 20\,\text{dB}$ at the resonant frequency of the mode TE_{101} ($f_{rTE_{101}} = 8.398\,\text{GHz}$).

higher frequencies, which is equivalent to reducing the cavity width considering $f_{TE_{101}} \approx \frac{c}{2a}$. From figure 2b, it can be concluded that the Q_0 parameter is also length independent for high d values.

The minimum accepted mode separation (mode clustering) depends on the measured quality factor, which in turn depends on the cavity shape, material, and quality of the manufacturing process. Larger Q_0s lead to sharper resonances, and hence modes can get closer in frequency without degradation. In general, in a conservative approach, we can expect that the unloaded quality factor of the fabricated prototype will be half of the theoretical value due to manufacturing tolerances in the fabrication process (roughness at inner walls, quality in soldering, metallic contact if screws are used). As a quantification of the mode clustering on the energy loss, in figure 3a, the form factor versus d/a for several Q_0 values is plotted. This plot shows that for high Q_0 values, the detriment in C is lower. The form factor in figure 3a has been computed with equation (1.2) taking into account

JHEP08(2023)098

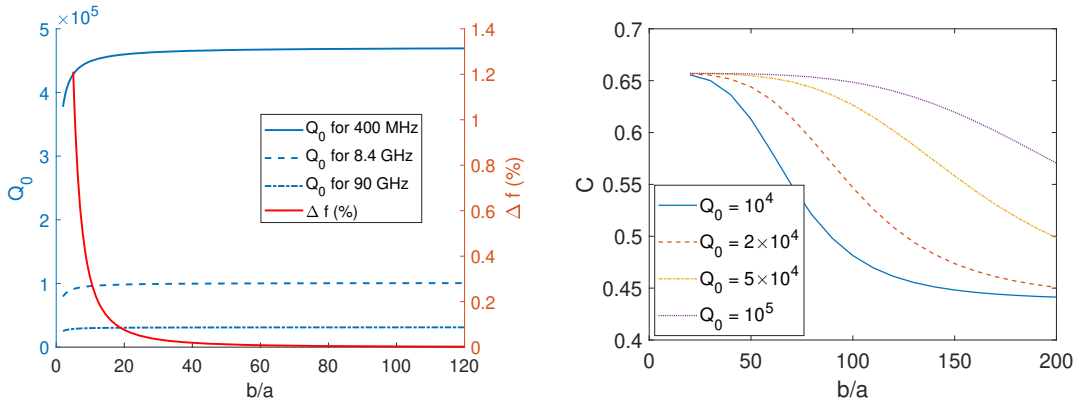

(a) **(b)**

Figure 4. (a) Q_0 of the TE_{101} mode as a function of b/a for three frequencies (0.4, 8.4, and 90 GHz) (blue lines), and relative mode separation between the modes TE_{101} and TE_{111}/TM_{111} of a single cavity as a function of b/a for $d = 28.55$ mm (X-band) (red line). (b) Form factor versus b/a for several Q_0 values.

the perturbation of the electric field (and thus its C detriment) due to the influence of the electric field of the next resonant mode (TE_{102} mode in this case) when they are very close. As a consequence of this behaviour, the electric field influence of the next mode is higher if the difference in the magnitude of the transmission parameter S_{21} of both resonances TE_{101} and TE_{102} at $f_{rTE_{101}}$ ($\Delta|S_{21}|$) is lower. In figure 3b, an example of two resonances with $Q_0 = 2 \times 10^4$ and $d = 1400$ mm (or $d/a \approx 79$) for 8.398 GHz is shown, which provides a form factor of $C = 0.65$. Thus, a limit must be imposed on the mode separation in order to obtain a minimum form factor.

2.2 Tall cavities

Similarly to the longitudinal dimension of a single resonant cavity, the vertical dimension b can be increased up to a limit imposed by the proximity of higher order modes (mode clustering between the TE_{101} and the TE_{111}/TM_{111}). In this case, the width a is not reduced because the resonant frequency does not change with b. With the increasing of the cavity height (b), the Q_0 value is increased up to a limit value, as shown in figure 4a (left axis). For completeness, in figure 4a (right axis), the frequency proximity with the nearest mode for X-band frequencies ($d = 28.55$ mm) is also represented. Similarly to the plot in figure 2a, this cavity shows a behaviour with a rapid decrease of the mode separation for high values of b/a.

To find the minimum accepted mode separation, a limit in C must be imposed again. The form factor versus b/a for several Q_0 values is plotted in figure 4b, taking into account that now the electric field contribution that affects negatively C comes from the TE_{111} mode. As was the case for long cavities, this plot shows that for high Q_0 values, the detriment in C is lower.

JHEP08(2023)098

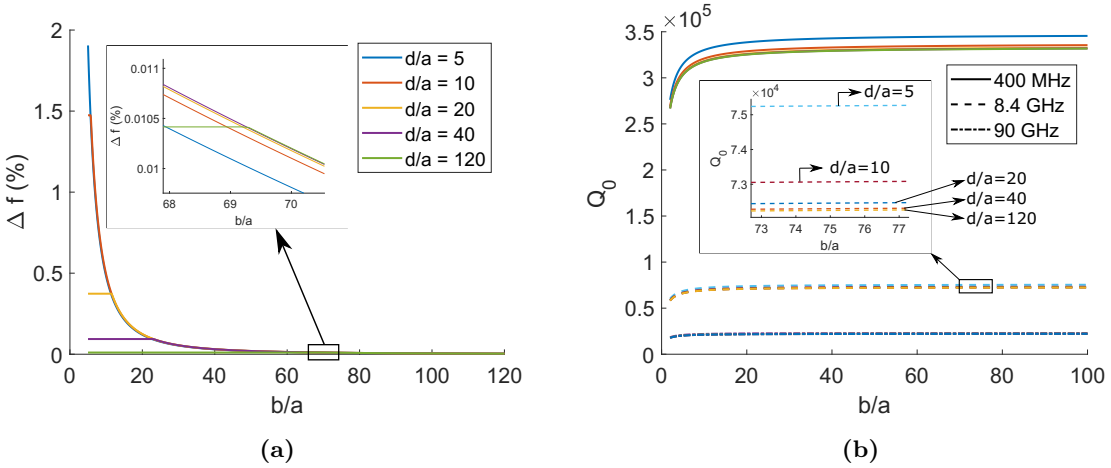

Figure 5. (a) Relative mode separation between the modes TE_{101} and TE_{102} or TE_{111}/TM_{111} (the closest one, depending on the b/a and d/a values) for X-band frequencies ($a = 17.85\,\text{mm}$). (b) Quality factor of the TE_{101} mode as a function of b/a for three frequencies (0.4, 8.4, and 90 GHz) for five d/a cases. In both pictures, the insets depict a zoom to differentiate all the d/a cases.

2.3 Large cavities

The last idea for increasing the volume of a single cavity is to increase both its length and height at the same time. The mode clustering problem now needs to consider two mode approximations to our working mode: TE_{102} (because of the longitudinal dimension d) and TE_{111}/TM_{111} (because of the vertical dimension b). The relative mode separation follows the behaviour from figure 5a, which shows the case for X-band frequencies ($a = 17.85\,\text{mm}$). The results show once again a rapid decrease in the mode separation when d/a and/or b/a increase.

The behaviour of the quality factor is depicted in figure 5b. For the X-band example, a width of $a = 17.85\,\text{mm}$ is necessary for maintaining $f_r = 8.4\,\text{GHz}$. For $d/a > 20$ and $b/a > 20$, the cavity provides a $Q_0 \approx 7.2 \times 10^4$, as shown in the inset of figure 5b. Note how the Q_0 is a bit lower as compared to the tall cavity because the width has been slightly reduced in order to compensate for the increase in length.

Again, in order to fix the minimum mode separation, a form factor limit should be established. The behaviour of the form factor with d/a, b/a, and Q_0 follows a similar pattern compared to figures 3a and 4b.

2.4 Comparison of long, tall, and large cavities

A form factor of $C = 0.65$ ($\sim 99\%$ of $C_{\text{max}} = 0.657$) is selected as our minimum acceptable reduced value due to mode clustering since it ensures the right measurement of the resonant frequency f_r and unloaded quality factor Q_0 in the experiment. Anyway, if the response of the cavity exhibits two resonances that are very close or even combined due to lower than expected quality factors, there are methods to extract the original shape of each resonance and compute the relevant two parameters (f_r and Q_0) [45]. The graphs in figure 3 help choose the guard frequency to avoid a high form factor detriment.

JHEP08(2023)098

Cavity type	a (mm)	b (mm)	d (mm)	Δf (%)	V (mL)	Q_0	C	Q_0VC (L)
Standard	22.86	10.16	28.55	38.3	6.63	4.6×10^4	0.657	200.37
Long	17.85	10.16	1400	0.024	253.9	3.9×10^4	0.65	6436.37
Tall	22.86	1500	28.55	0.007	978.98	10^5	0.65	6.4×10^4
Large	17.85	1100	1600	0.013	3.14×10^4	7.2×10^4	0.65	1.47×10^6

Table 2. Comparison of the operational parameters of a standard WR-90 rectangular cavity employed for resonating at 8.4 GHz with very long, tall, and large cavities for the same resonant frequency. In addition, the distance between the axion mode and its first neighbour (Δf) is added for each case.

For the X-band case, this form factor minimum value is achieved with the dimensions shown in table 2. These values have been calculated assuming an unloaded quality factor after fabrication of half of the theoretical one. Table 2 also shows the improvements obtained with these three cases in comparison with a WR-90 rectangular cavity. In the case of a very large cavity, the Q_0VC factor of 7336 is a considerable improvement over the conventional WR-90 cavity.

It can be observed in table 1 that the long cavity fits perfectly in a dipole magnet like CAST. However, for a solenoid magnet, the cavity length should be reduced to fit the bore diameter. For example, in MRI (ADMX-EFR), a maximum length of $d \approx \phi_{\text{MRI}} = 800\,\text{mm}$ is imposed since the longitudinal axis of the cavity should be oriented along any radial axis of the solenoid magnet (see figure 1a) due to its magnetic field direction. In this case, there is a lot of unused space along the longitudinal axis of the solenoid magnet (z-axis in figure 1a). Anyway, the increased volume from a standard cavity is still high.

Focusing on table 1, it can be observed how the height of tall cavities has to be decreased until it fits into the longitudinal axis of a solenoid magnet. For example, in MRI (ADMX-EFR), a maximum height of $b = L_{\text{MRI}} = 513\,\text{mm}$ is imposed. Anyway, the volume gained from a standard cavity is again very high. For a dipole magnet, the only option to have a substantial benefit is BabyIAXO, whose $\phi_{\text{BabyIAXO}} = 600\,\text{mm}$ diameter bore can be used to fit this tall structure in the radial orientation (y-axis in figure 1b). With this scenario, there is a lot of unused space on the longitudinal axis of this magnet (z-axis in figure 1b), that can also be exploited with the novel ideas proposed in the next sections.

Also, it can be seen that in dipole magnets, the best orientation for large cavities is obtained by matching both the longitudinal axis of the cavity and the magnet bore since they have the highest dimension values and both the electric field of the cavity and the magnetic field of the magnet are aligned. For example, in BabyIAXO, the vertical cavity dimension can be increased until $b = 600\,\text{mm}$ (y-axis in figure 1b), and the length can be extended to its limit $d = 1600\,\text{mm}$ (z-axis in figure 1b), which with $a = 17.85\,\text{mm}$ gives a volume of $V = 1.71 \times 10^4\,\text{mL}$ representing an improvement of 2580 in volume compared with a standard WR-90 cavity. For a solenoid magnet, the height dimension must match the longitudinal axis of the bore (z-axis in figure 1a), and the haloscope length can occupy all the bore diameter. For example, at the MRI (ADMX-EFR) solenoid magnet, a haloscope of $a = 17.85\,\text{mm}$, $b = 513\,\text{mm}$, and $d = 800\,\text{mm}$, which implies a volume of $V = 7326\,\text{mL}$,

JHEP08(2023)098

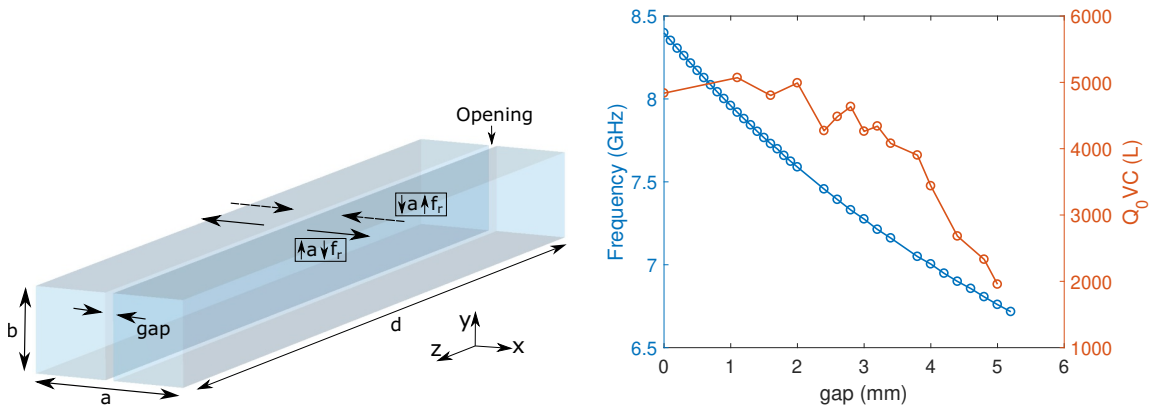

(a) **(b)**

Figure 6. (a) 3D model of a long cavity with vertical cut tuning, and (b) frequency tuning (blue line) and Q_0VC factor (red line) versus vertical cut opening gap of a cavity with dimensions $a = 17.85\,\text{mm}$, $b = 10.16\,\text{mm}$, and $d = 1000\,\text{mm}$.

could be installed. This means reducing the volume by half compared to the BabyIAXO dipole magnet scenario. However, this reduction can be compensated by the lower working temperature (lower T_{sys} in equation (1.1)) and higher magnetic field values employed in ADMX (see table 1).

2.5 Vertical cut tuning

As a proof of concept, tuning studies have been carried out using the vertical cut method, previously used by the RADES group [46] (see figure 6a), in a long cavity of $d = 1000\,\text{mm}$ to observe its behaviour against mode separation and figure of merit Q_0VC. Figure 6b shows the frequency tuning and the associated figure of merit achieved for this cavity by applying a vertical aperture gap of 0 to 5 mm. By setting a minimum Q_0VC factor limit of ≈ 3900, it can be stated that a tuning range of 1349 MHz (17.47%) is obtained, which corresponds to an excellent result [46]. The mode separation remains almost constant for the whole range. More tuning studies for cavities with large dimensions are expected to be carried out as a future line of this work by adapting the mechanical and electronic systems developed by the RADES group in [46] and [47], respectively.

3 1D multicavities

The multicavity concept in rectangular haloscopes allows for an increase in volume along the longitudinal axis without decreasing the resonant frequency [22]. In contrast to the long cavity concept, z-axis multicavity designs can make use of wider rectangular waveguides (for example, WR-90 for X-band). On the other hand, a first successful high-efficiency and high-frequency resonator was manufactured and operated at CAPP, making use of a multiple-cell cavity approach with cylindrical geometries, which allows the increase of the whole volume in haloscopes without lowering the operation frequency, similarly to the

JHEP08(2023)098

multicavity idea [48, 49]. In addition, in this same research group within the CAST-CAPP project, the development of phase-matched rectangular cavities has been carried out to search for axions around 5 GHz [25].

Several small haloscope prototypes with rectangular geometries have been designed and manufactured up to now by the RADES group. Among them, an all-inductive structure based on five subcavities and two alternating structures with two different numbers of subcavities ($N = 6$ and $N = 30$, where N is the number of subcavities). Details and results of the first two structures are presented in [19, 22, 46, 50, 51].

For the design of the multicavity haloscopes, the coupling matrix is employed as a supporting tool. The theoretical concepts of this method can be found in [50, 52]. In the case of 1D multicavities, the following matrix has been employed for the development of the geometrical parameters in the studied structures of this work:

$$\mathbf{M} = \begin{pmatrix} \Omega_1 & M_{1,2} & 0 & 0 & \cdots & 0 & 0 & 0 \\ M_{1,2} & \Omega_2 & M_{2,3} & 0 & \cdots & 0 & 0 & 0 \\ 0 & M_{2,3} & \Omega_3 & M_{3,4} & \cdots & 0 & 0 & 0 \\ 0 & 0 & M_{3,4} & \Omega_4 & \cdots & 0 & 0 & 0 \\ \vdots & \vdots & \vdots & \vdots & \ddots & \vdots & \vdots & \vdots \\ 0 & 0 & 0 & 0 & \cdots & \Omega_{N-2} & M_{N-2,N-1} & 0 \\ 0 & 0 & 0 & 0 & \cdots & M_{N-2,N-1} & \Omega_{N-1} & M_{N-1,N} \\ 0 & 0 & 0 & 0 & \cdots & 0 & M_{N-1,N} & \Omega_N \end{pmatrix}, \tag{3.1}$$

where $M_{i,j}$ are the impedance inverter values in the normalised low-pass prototype network and Ω_q is the difference of the resonant frequency in the q-th subcavity with respect to the axion frequency [52]. $M_{i,j}$ is related to the physical interresonator coupling k selected in the design. In order to extract its value, a low-pass to band-pass transformation ($\Omega = \left(\frac{f}{f_{\text{axion}}} - \frac{f_{\text{axion}}}{f}\right)\frac{1}{f_B}$, where $f_B = \frac{BW}{f_{\text{axion}}}$ is the fractional bandwidth and BW the bandwidth) is usually carried out [52]. In this paper, a bandwidth of $BW = 100$ MHz is employed for all the multicavity designs. With these considerations, the relationship with the coupling value is given by [52]:

$$M_{i,j} = \frac{k_{i,j}}{f_B}, \tag{3.2}$$

where $k_{i,j}$ is the physical coupling value between the resonators i and j. More details about these parameters can be found in [52]. The Ω_q values can be extracted with the condition $\mathbf{M} \times \mathbf{1}_N^T = \mathbf{0}_N^T$, where $\mathbf{1}_N$ is a 1-vector of size N and $\mathbf{0}_N$ is a 0-vector of size N [50, 52]. The matrix dimension ($N \times N$) depends on the number of subcavities. In addition, as can be seen, the values of the elements outside the three main diagonals of the matrix are zero. This translates into the fact that resonators that are not contiguous have no physical coupling.

At first glance, it might be thought that there would be no problem with resonant mode clustering since the TE_{102} mode is far away as it has a small subcavity length. However, the multicavity structure introduces additional resonant modes that are associated with the eigenmodes of the coupled cavity system, the so-called *configuration modes* [50]. These configuration modes exist for any TE_{mnp} resonant mode. Their resonant frequencies become closer to the axion eigenmode as the number of subcavities increases and the inter-resonator coupling value k decreases. The theory and extraction methods of the physical

JHEP08(2023)098

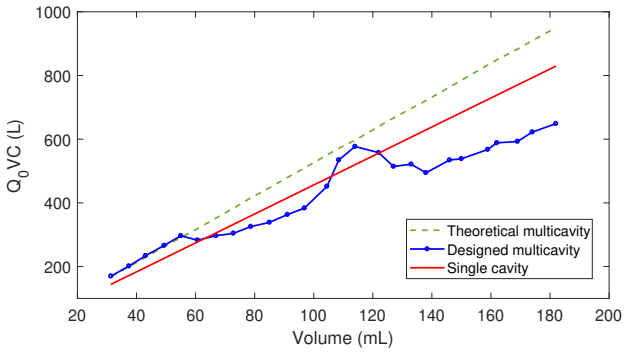

Figure 7. Figure of merit Q_0VC of a large single cavity versus both theoretical and designed multicavity structures. Each dot at the designed multicavity line (blue line) corresponds with a different number of subcavities, from left to right: $N = 5$ to 30 subcavities. The first case ($N = 5$) corresponds with the first RADES haloscope, whose behaviour is detailed in [50].

coupling k can be found in [51]. The number of configuration modes of the coupled cavity system for each TE_{mnp} mode is equal to the number of subcavities.

Due to the loading effect of a coupling window [52], higher interresonator couplings lead to shorter subcavity lengths in order to keep the same resonant frequency. This effect is small for the frequency of our examples (8.4 GHz), where the lengths could vary around 1 or 2 mm. However, for very high k values, the iris windows need to be opened significantly, leading to a substantial loading effect. For other frequency bands like UHF, this effect will have to be taken into account even for relatively low values of k. Once again, there is a trade-off between volume and mode separation. Figure 7 shows an 8.4 GHz example that compares the figure of merit (Q_0VC) of both single and multicavity designs (with $|k| = 0.0377$, a similar value to the one usually employed in [51]) as a function of the total volume (increasing the length d for the single cavity case and increasing the number of cavities N for the multicavity case).[2] All the simulation results in this work were obtained from the Computer Simulation Technology (CST) Studio Suite software [53] in the Frequency Domain.

The multicavity design procedure is based on the following steps: first, the working frequency or axion search frequency (for the TE_{101} mode in our case) and a physically realisable interresonator coupling k are chosen [50]. Secondly, the coupling matrix method is applied as described in [50], which gives the natural frequencies of each subcavity of the array. Finally, an iterative optimisation is carried out in which the subcavities are tuned to resonate at the correct frequency and the irises are adjusted to provide the chosen physical coupling.

Instabilities in the design results are observed due to the high sensitivity of the form factor during the optimisation process, which becomes more complex with an increase in the number of cavities (as depicted in figure 7). Overcoming these difficulties would result in an improvement similar to the theoretical multicavity curve, which is better than the

[2] A similar study could be done comparing both single and multicavity structures but increasing the height b and the number of cavities N in the vertical direction, respectively.

JHEP08(2023)098

improvement that can be obtained with a single cavity, and, therefore, the multicavity concept seems the best option for improving the sensitivity of the axion detection system. Regarding the quality factor, it is inferred from figure 7 that it is independent of the number of subcavities. For this comparison, the multicavity has a slightly higher value because a standard width of $a = 22.86\,\text{mm}$ is being used (for the single long cavity design, it has to be reduced to $a = 17.85\,\text{mm}$) and the Q_0 depends strongly on this dimension. Under these considerations (see table 2), for $a = 22.86\,\text{mm}$, the quality factor takes values around 4.6×10^4, and for $a = 17.85\,\text{mm}$, it is $Q_0 \approx 3.9 \times 10^4$. Therefore, the difference in the slope of the Q_0VC behaviour between single cavities and multicavities is given by Q_0.

The structures based on the multicavity technique must guarantee the synchrony of the electromagnetic field of the operation mode at all the subcavities. This synchrony can be altered due to manufacturing errors due to mechanical tolerances, producing higher field levels in some subcavities and lower ones in others (which can lead to a reduction in the form factor). The RADES group has carried out tolerance studies for this type of structure, giving rise to satisfactory results for deviations of +/− 30 microns, which are considered acceptable values for manufacturing tolerances in these structures [51]. It is assumed that all the haloscopes studied in this paper will follow a behaviour very similar to that of the previous contribution.

Regarding the mode clustering issue, there is a solution to shift the neighbour configuration modes of the TE_{101} mode away from the axion one for the multicavity designs. This procedure is based on alternating the signs of the couplings, which is practically achieved by using the two types of irises (capacitive or horizontal window and inductive or vertical window) as discussed in [51]. For an all-inductive design ($k < 0$), the axion mode corresponds with the first configuration of the TE_{101} mode, and for an all-capacitive haloscope ($k > 0$), it corresponds with the last one. However, for an alternating inductive/capacitive structure, the axion mode will be the central one (when there is an odd number of cavities) or the mode in the position $\frac{N}{2} + 1$ (when there is an even number of cavities), where the distance between the configuration modes is higher. Figure 8a plots an example of the S_{21} magnitude as a function of the frequency for the three previous cases (all-capacitive, all-inductive, or alternation of both types of irises) in a multicavity based on six subcavities with $|k| = 0.0377$. As can be seen, the all-inductive and all-capacitive multicavities provide the axion mode at their first and last resonances, respectively, while for the alternating structure it is positioned in the position $\frac{N}{2} + 1 = 4$. In figure 8b[3] the relative mode separation between the closest configuration mode and the axion one is observed for these three cases plus the single long cavity case in an X-band structure. Also, in figure 8c, the dependency of the relative mode separation with the physical coupling value is plotted. In addition, the behaviour of increasing the volume with different $|k|$ values and types can be observed in figure 8d. The results of the multicavity case in these plots have been generated with the formulation described in [50] (for the all-inductive/capacitive case) and [51] (for the alternating case).

[3]For this plot, a reasonable assumption has been made for the multicavity case: same subcavity volume for any N. In practise, the difference in length is minimal during the calculation of the final volume, which is the parameter that is represented in this plot.

JHEP08(2023)098

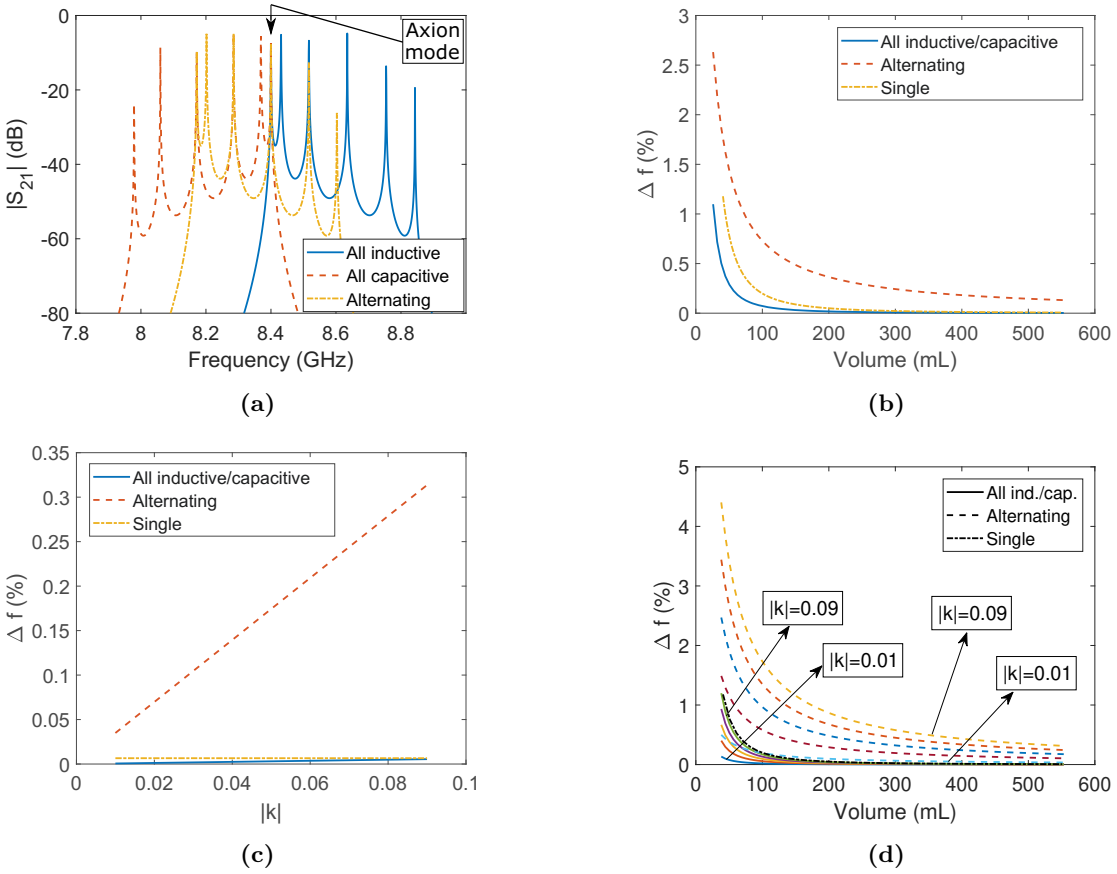

Figure 8. Comparison of all-inductive irises, all-capacitive irises, and alternating inductive/capacitive irises for a design example working at 8.4 GHz with $|k| = 0.0377$: (a) magnitude of S_{21} as a function of the frequency for a 6-subcavities multicavity of each type, (b) relative mode separation between the closest eigenmode to the axion one versus volume, (c) relative mode separation versus the absolute value of the physical coupling k for $N = 90$, and (d) relative mode separation between the closest mode to the axion one versus volume for several physical coupling values and types. For the all-inductive/capacitive and alternating cases, several $|k|$ values have been used (from bottom to top: $|k| = 0.01$, 0.03, 0.05, 0.07, and 0.09). The single long cavity case has been added in (b), (c), and (d) for comparison. In (c), a single cavity length of $d = 2700\,\text{mm}$ has been employed in order to produce the same volume as the multicavity.

As can be seen in figure 8b, the alternating concept provides a great improvement in terms of mode separation. However, the manufacturing of mixed capacitive and inductive irises is complicated, which makes the construction of alternating multicavities more difficult as compared with the all-inductive multicavity case. Also, although the largest frequency separations are achieved with the highest values of $|k|$, as depicted in figures 8c and 8d, in the practical design of multicavity haloscopes, intermediate values of physical coupling are chosen so that the loading effect of the couplings does not reduce the subcavity lengths excessively, as reported previously [50].

JHEP08(2023)098

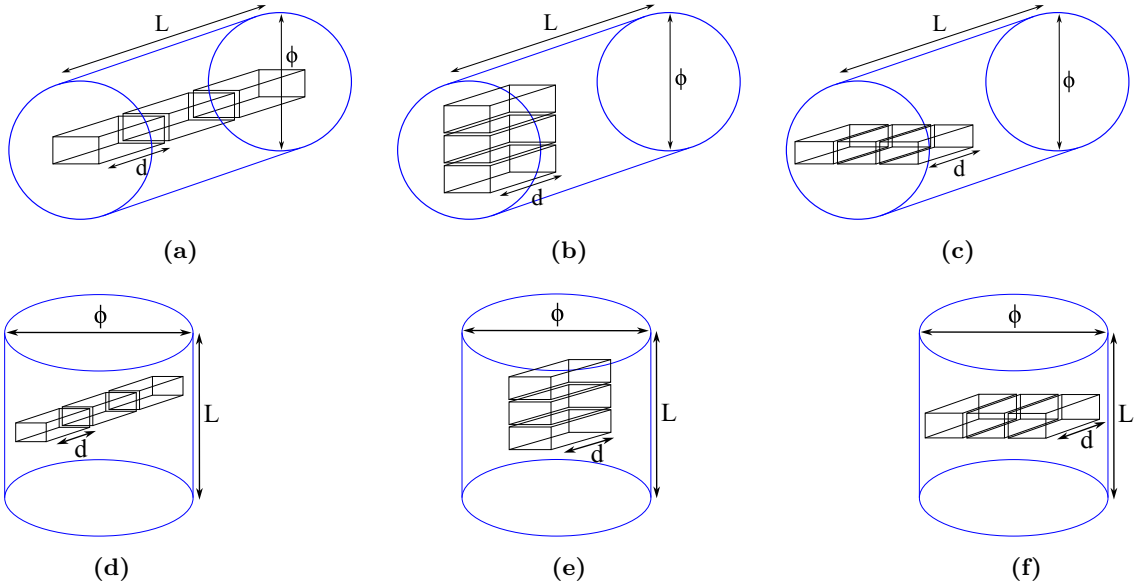

Figure 9. Implementation of three long subcavities stacked in different directions in dipole and solenoid magnets. For dipole magnets: (a) in length, (b) in height, and (c) in width. For solenoid magnets: (d) in length, (e) in height, and (f) in width. Although it is not presented in these sketches, it is assumed that for each multicavity design, the readout antenna will be positioned on the upper wall of the first subcavity.

Another advantage of the multicavity concept compared with single cavities is that the extraction of the RF power (with a coaxial to waveguide transition, for example) in a critical coupling regime or overcoupled regime is easier. This is because in a multicavity structure, there is a maximum value of the electric field in each subcavity for the resonant mode, whereas in a single cavity, there is only one maximum inside the whole structure. For multicavities, the concentration of the electric field in the centre of the subcavities decreases with higher $|k|$. Thus, another trade-off between the relative mode separation (requiring high $|k|$) and the extraction of the coupling power (more efficient with low $|k|$) is found here.

3.1 Long subcavities

The combination of both long and multicavity concepts can be considered a novel concept for taking advantage of the volume available in the bore of a dipole or solenoid magnet. This principle is based on increasing the length of the subcavities in the multicavity array while decreasing slightly the width to maintain the correct operational frequency. As previously explained, reducing the width of the subcavities results in a slight decrease in the quality factor.

There are three possibilities for coupling (or stacking) the subcavities in a 1D multicavity structure: in length, in height, or in width. From figure 9a to figure 9f,[4] examples

[4]Note here how, for solenoid magnets, the vertical direction of the multicavity is now oriented towards the longitudinal direction of the bore (this is, z-axis in figure 1a) to align the electric field of the haloscope with the static magnetic field of the magnet.

JHEP08(2023)098

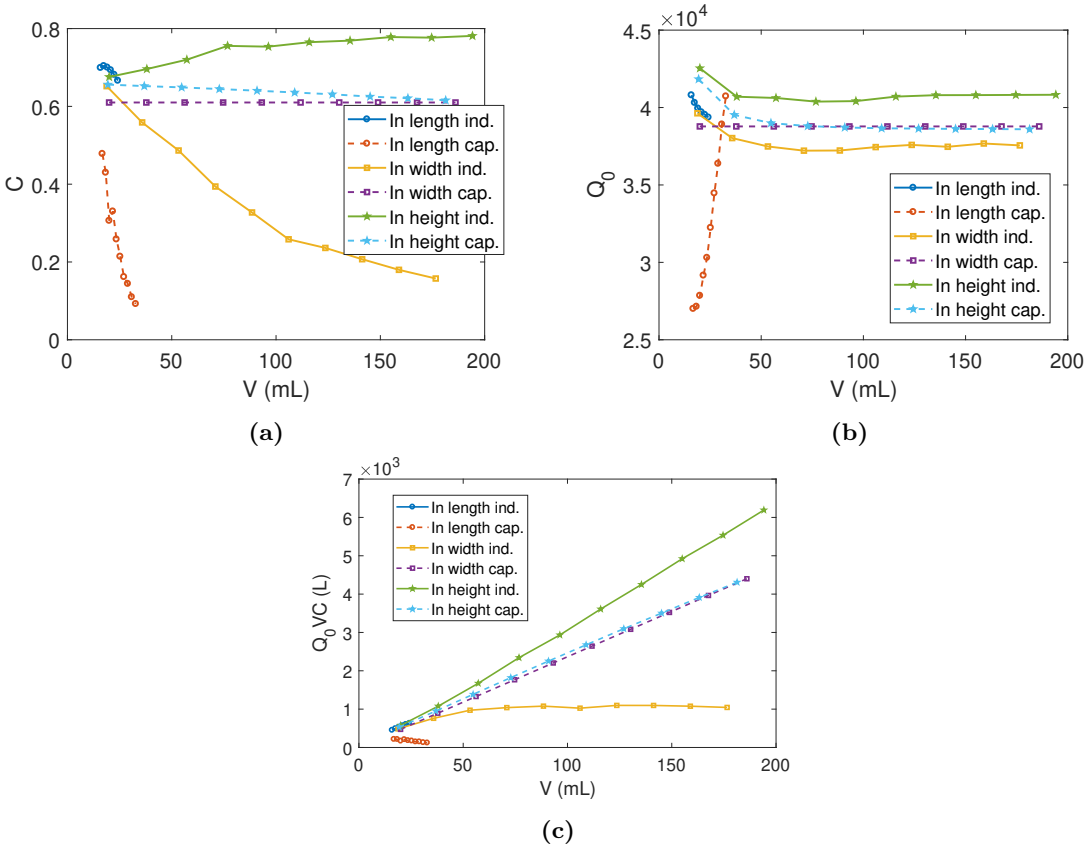

Figure 10. Influence on the design parameters of each type of coupling (inductive or capacitive) when the coupling is introduced along each direction (longitudinal (length), horizontal (width), or vertical (height)) in a structure composed of two coupled long subcavities (with $b = 10.16\,\text{mm}$ and $a = 17.85\,\text{mm}$) working at X-band: (a) form factor, (b) quality factor, and (c) Q_0VC figure of merit. The volume depends only on the length, as the number of subcavities is fixed at two.

with three long subcavities for each type of stacking in both dipole and solenoid magnets are shown. For multicavities stacked in length using the z-axis, longer subcavities lead to lower coupling values $|k|$ as energy decays on the way to the irises. There is a limit to subcavity length where the irises cannot provide the correct coupling value, making very large subcavities impossible. Indeed, for solenoid magnets, using the length for stacking is not ideal due to diameter limitations, but other stacking directions have more freedom in length. There are limitations for stacking in height or width for both dipoles and solenoids due to bore size. For example, in solenoids, if a square area footprint is desired, a maximum $d = \frac{\phi}{\sqrt{2}}\,\text{mm}$ value should be implemented. A more efficient geometry could be used with different subcavity lengths to increase haloscope volume. Additionally, the number of subcavities and the subcavity length are also limited by mode clustering, according to figure 8b.

Figure 10 shows a comparison study of these three types of coupling directions for X-band in a two-subcavities structure employing an inductive or capacitive iris varying the volume, which depends only on the subcavity length since the height ($b = 10.16\,\text{mm}$), the

JHEP08(2023)098

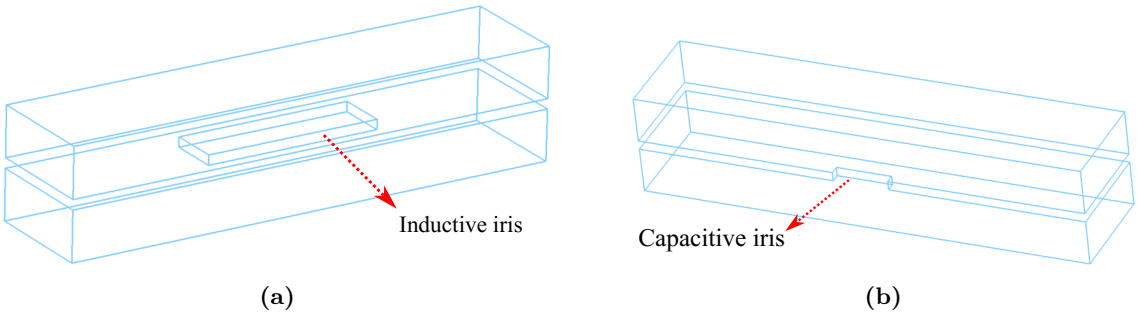

Figure 11. Sketch of a multicavity based on two subcavities stacked in height employing (a) an inductive iris, and (b) a capacitive iris.

width ($a = 22.86\,\text{mm}$), and the number of subcavities ($N = 2$ for simplicity) are fixed. These results are valid for both dipole and solenoid magnets as long as the approximation of $\vec{B}_e = B_e\,\hat{y}$ for dipoles and $\vec{B}_e = B_e\,\hat{z}$ for solenoids is accomplished. In that case, the form factor C is equal in both situations.

A coupling value of $|k| = 0.025$ is used for this study, which is a typical value employed in RADES. Figure 10 shows how, for the in length coupling option, the curves (both inductive and capacitive) are limited to volume values lower than 50 mL. This is due to the length limitation in the subcavities for this kind of coupling direction, as previously explained (the required coupling $|k| = 0.025$ cannot be obtained with larger lengths). For the other four curves, there is no such limitation, so this study can be continued with higher volumes if necessary. Analysing the Q_0VC plot in figure 10c, it can be seen that the in height coupling is the best option for long subcavities. However, depending on the type and dimensions of the magnet, the x-axis direction option could be more appropriate.

For the in height coupling, it is not obvious how to design an inductive/capacitive iris. For this reason, a previous study varying the position and dimensions of a rectangular window has been carried out to find the inductive and capacitive behaviours. For an inductive operation, the window is positioned at the centre of the subcavity in a rectangular shape (see figure 11a). For a capacitive iris, it is displaced to one side along the width with a thin rectangular shape (see figure 11b).

All these studies have been carried out for the all-inductive and all-capacitive multicavity cases. However, as seen previously, the alternating case is the one that provides the largest frequency separation between adjacent modes. Therefore, as a proof of concept, an alternating multicavity haloscope coupled in the vertical axis and based on $N = 4$ long subcavities of $d = 100\,\text{mm}$ has been designed.

The selected physical $|k|$ value for the interresonator couplings is 0.025, and the resulting coupling matrix (using equation (3.2)) is:

$$\mathbf{M} = \begin{pmatrix} -0.5 & 0.5 & 0 & 0 \\ 0.5 & 0 & -0.5 & 0 \\ 0 & -0.5 & 0 & 0.5 \\ 0 & 0 & 0.5 & -0.5 \end{pmatrix}, \tag{3.3}$$

which has been employed for the design of the structure with the methods described in [50, 52]. Considering the non-zero off-diagonal elements, an alternating behaviour can

JHEP08(2023)098

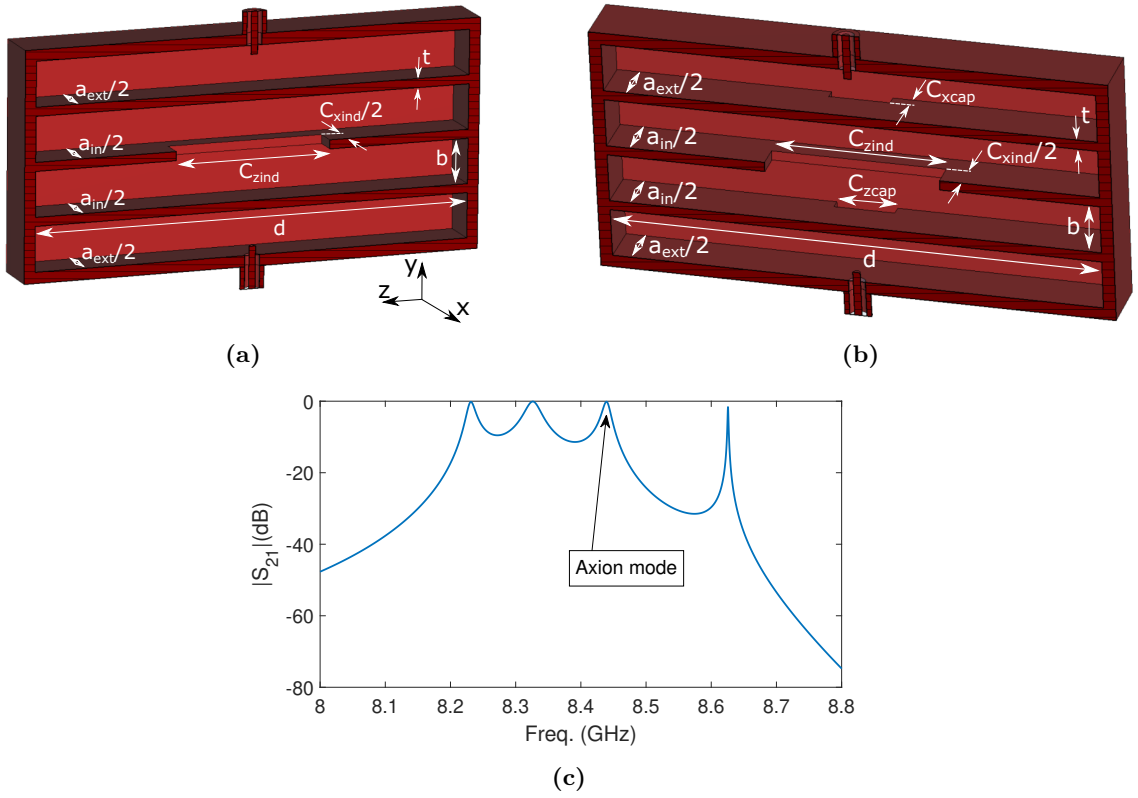

Figure 12. Alternating 1D vertically-coupled multicavity haloscope design based on four long subcavities with two capacitive and one inductive irises: (a) left piece of the structure, (b) right piece of the structure, and (c) S_{21} magnitude as a function of the frequency.

be observed (positive sign for capacitive couplings and negative for inductive couplings).

Figures 12a and 12b show the final aspect of the haloscope, evidencing the geometry and position of each type of coupling in this kind of multicavity (subcavities stacked in height). In figure 12c the simulated S_{21} magnitude as a function of the frequency is shown.

The dimensions of the structure according to figures 12a and 12b are: length (z-axis) and height (y-axis) of all the subcavities $d = 100\,\text{mm}$ and $b = 10.16\,\text{mm}$, respectively; internal subcavities width $a_{\text{in}} = 18.3\,\text{mm}$ (x-axis); external subcavities width $a_{\text{ext}} = 17.9\,\text{mm}$; capacitive iris length $C_{\text{zcap}} = 12.4\,\text{mm}$ (z-axis); capacitive iris width $C_{\text{xcap}} = 2\,\text{mm}$ (x-axis); inductive iris length $C_{\text{zind}} = 35.5\,\text{mm}$; inductive iris width $C_{\text{xind}} = 10\,\text{mm}$, and thickness of all the irises $t = 2\,\text{mm}$ (y-axis). The capacitive windows are positioned at one side in width (x-axis) and centred in length (z-axis), while the inductive window is placed at the centre both in width and length of the subcavities.

As can be seen, the number of resonances for the TE_{101} mode is four, which, as expected, matches the number of subcavities (four configuration modes of the TE_{101} resonance in the coupled cavity system). If the magnitude of the electric field of these four eigenmodes (see figure 13) is observed, the axion mode is identified as the third one (the one with all the subcavities in synchrony [51]), verifying the alternating behaviour (since there is an even number of subcavities).

JHEP08(2023)098

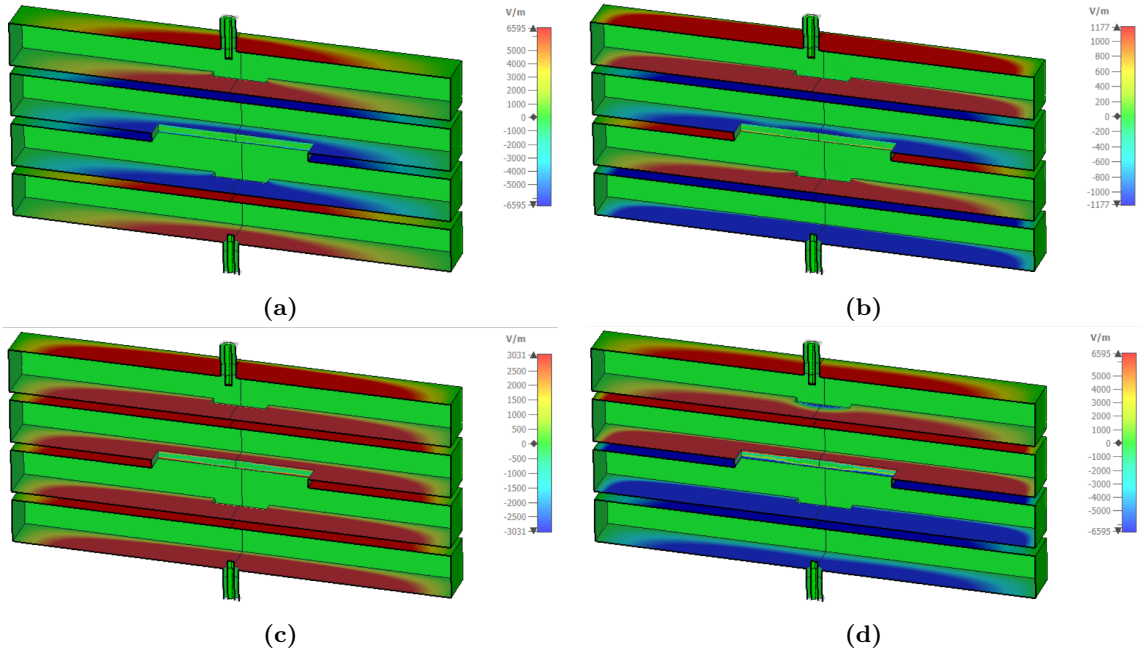

Figure 13. Magnitude of the electric field of the configuration modes in the structure shown in figure 12: (a) [+ − − +], (b) [+ − + −], (c) [+ + + +], and (d) [+ + − −], where "+" and "−" represent a positive and negative E-field level in each subcavity, respectively.

Due to the low number of subcavities used ($N = 4$), the relative mode separation of this structure ($\Delta f = 1.3\%$ or 113 MHz) is far from our limits. The proximity of the next resonant mode (TE_{102}) is not a relevant issue because it is even further in frequency (and outside the frequency range represented) due to the moderate d value.

The resonant frequency of the axion mode is $f = 8.439$ GHz, which is a good result compared to the goal of 8.4 GHz. The quality and form factors are $Q_0 = 39579$ and $C = 0.654$, respectively, which is in line with the results from figure 10 for the vertical coupling option in inductive and capacitive irises for lengths of $d = 100$ mm ($V \approx 37$ mL for two subcavities). This validates the theoretical analysis presented in this section. The resulting total volume of the haloscope is $V = 74$ mL, and the total Q_0VC is 1915.47 L, which is 9.56 times higher than a single standard WR-90 cavity.

3.2 Tall subcavities

According to section 2.2, tall structures, especially 1D multicavity structures, can enhance the volume of haloscopes. Figures 14a–14f show three different forms of stacking in a multicavity with three tall subcavities in dipole and solenoid magnets. Tall subcavities stacked in length have a constraint in the b value due to the bore diameter, but tall subcavities stacked in height and width have a constraint in both the b and N values. The tall multicavities stacked in width scenario for dipoles is equivalent to the long subcavities stacked in width scenario for solenoids. A more efficient shape could be implemented with different subcavity heights to increase multicavity volume. For solenoid magnets, a limitation in the b and N values is found for the tall subcavities stacked in length

JHEP08(2023)098

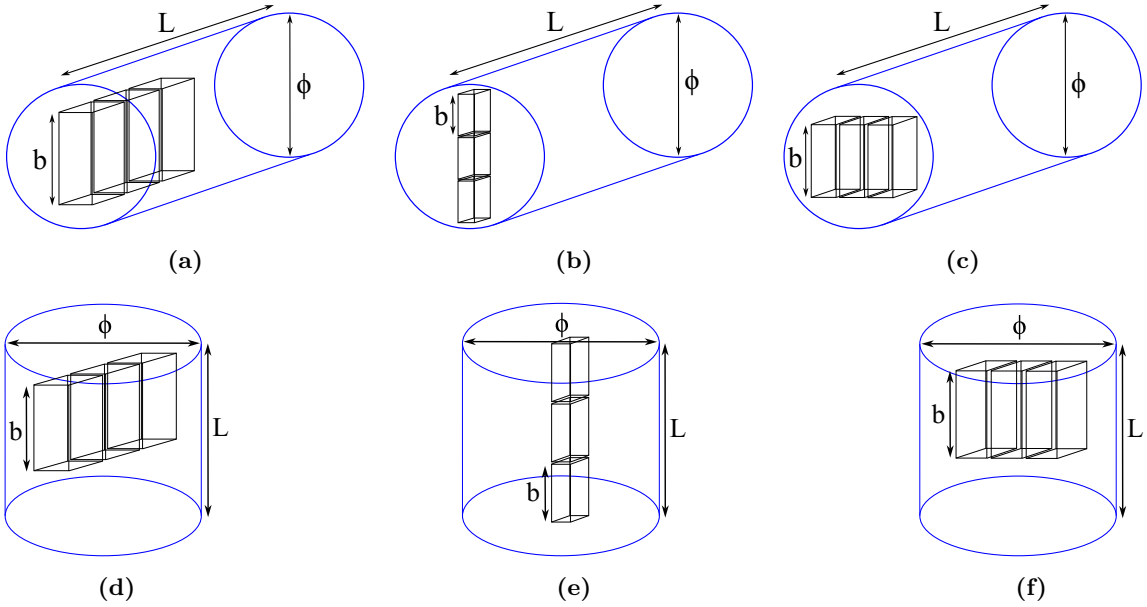

Figure 14. Implementation of three tall subcavities stacked in different directions in dipole and solenoid magnets. For dipole magnets: (a) in length, (b) in height, and (c) in width. For solenoid magnets: (d) in length, (e) in height, and (f) in width.

and in width because of the magnet height and diameter, respectively. Also, for tall subcavities stacked in height, a limitation in the b and N values is imposed due to the solenoid bore height.

Regardless of the magnet dimensions, the limit in the number of subcavities N and in the subcavity height b is imposed by the same criteria as the single cavities (as was the case for long multicavities): the mode separation described in section 2.1, but according to the results provided in figure 8b.

Figure 15 shows the results of a study conducted for coupling in three axes with a coupling value of $|k| = 0.025$ and increasing subcavity height in a $N = 2$ subcavity prototype. The outcomes reveal that in height coupling with inductive iris has a high limit and a volume limit of $V \approx 50\,\text{mL}$ for the correct coupling value, similar to in length coupling with long subcavities. For tall subcavities, in length and in width coupling with inductive irises, and in height coupling with capacitive irises are the best options. An all-inductive 1D multicavity of $N = 4$ tall subcavities with $b = 300\,\text{mm}$ employing in length stacking was designed (see figure 16a), which could operate at BabyIAXO dipole and MRI solenoid magnets. Again, the selected $|k|$ value for the physical couplings is 0.025 and the extracted coupling matrix is:

$$\mathbf{M} = \begin{pmatrix} 0.5 & -0.5 & 0 & 0 \\ -0.5 & 1 & -0.5 & 0 \\ 0 & -0.5 & 1 & -0.5 \\ 0 & 0 & -0.5 & 0.5 \end{pmatrix}. \tag{3.4}$$

The signs of the M_{12}, M_{23}, and M_{34} elements (and their symmetrical pairs) are negative because the structure is based on all inductive irises.

JHEP08(2023)098

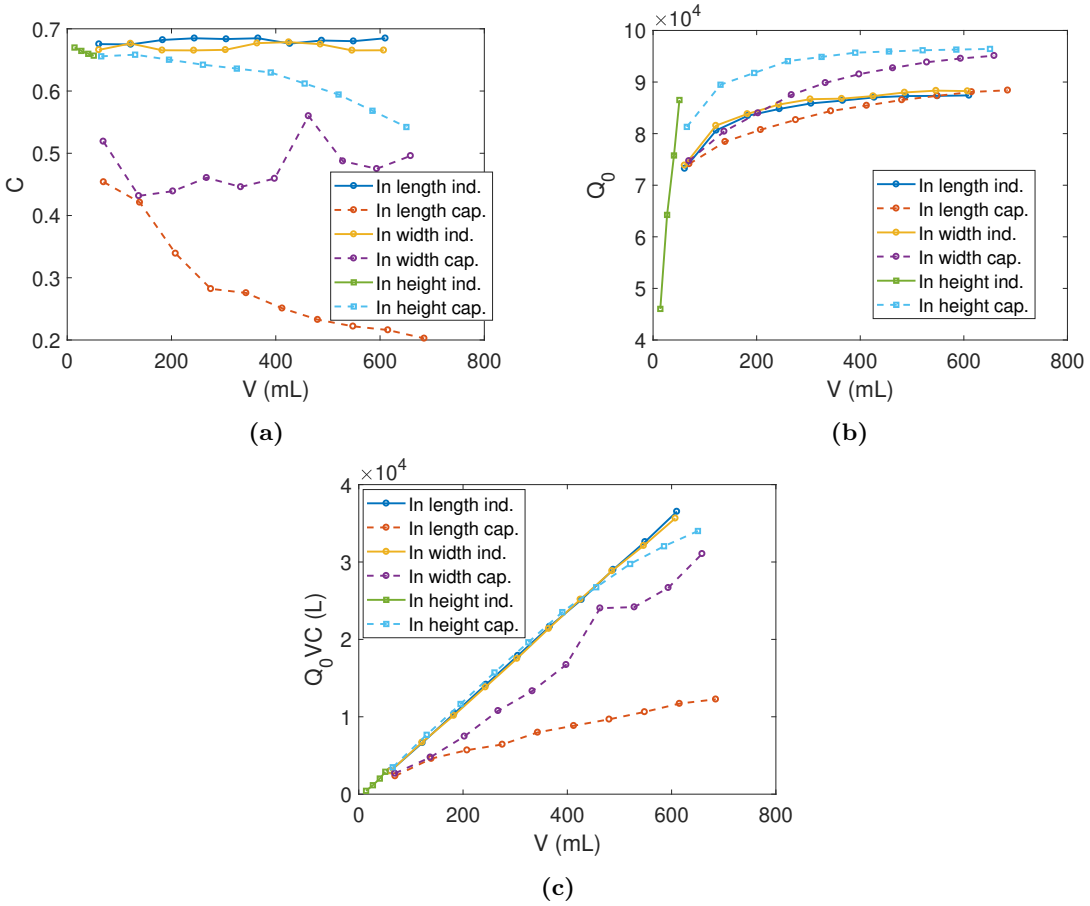

Figure 15. Influence on the design parameters of each type of coupling (inductive or capacitive) when the coupling is introduced along each direction (in length, in width, and in height) in a structure composed of two coupled tall subcavities working at X-band: (a) form factor, (b) quality factor, and (c) Q_0VC figure of merit. The volume depends only on the height, as the number of subcavities is fixed at two.

In figure 16b a picture of the manufactured prototype is shown. Figure 16c plots the S_{21} magnitude as a function of the frequency for both simulation and measurements, which are in good agreement.

The dimensions of the prototype are: height and width of all the subcavities $b = 300\,\text{mm}$ and $a = 22.86\,\text{mm}$, respectively, internal subcavities lengths $d_{\text{in}} = 26\,\text{mm}$, external subcavities lengths $d_{\text{ext}} = 27\,\text{mm}$, inductive width $a_i = 9\,\text{mm}$, and thickness of the irises $t = 2\,\text{mm}$. The total dimensions of the haloscope, taking into account the external copper thickness of $t_{Cu} = 5\,\text{mm}$, are width $a_h = 32.86\,\text{mm}$, height $b_h = 310\,\text{mm}$, and length $d_h = 122\,\text{mm}$.

From simulations, considering copper walls, a quality factor value of $Q_0^{2K} = 76000$ is obtained for the axion mode (at 8.227 GHz) at cryogenic temperatures and $Q_0^{300K} = 13200$ at room temperature. The measurements from the manufactured structure provide a value of $Q_0^{300K} = 7300$ (55.3% of the simulation result), which corresponds with a typical reduction of manufactured Q_0 compared with other RADES structures [50].

JHEP08(2023)098

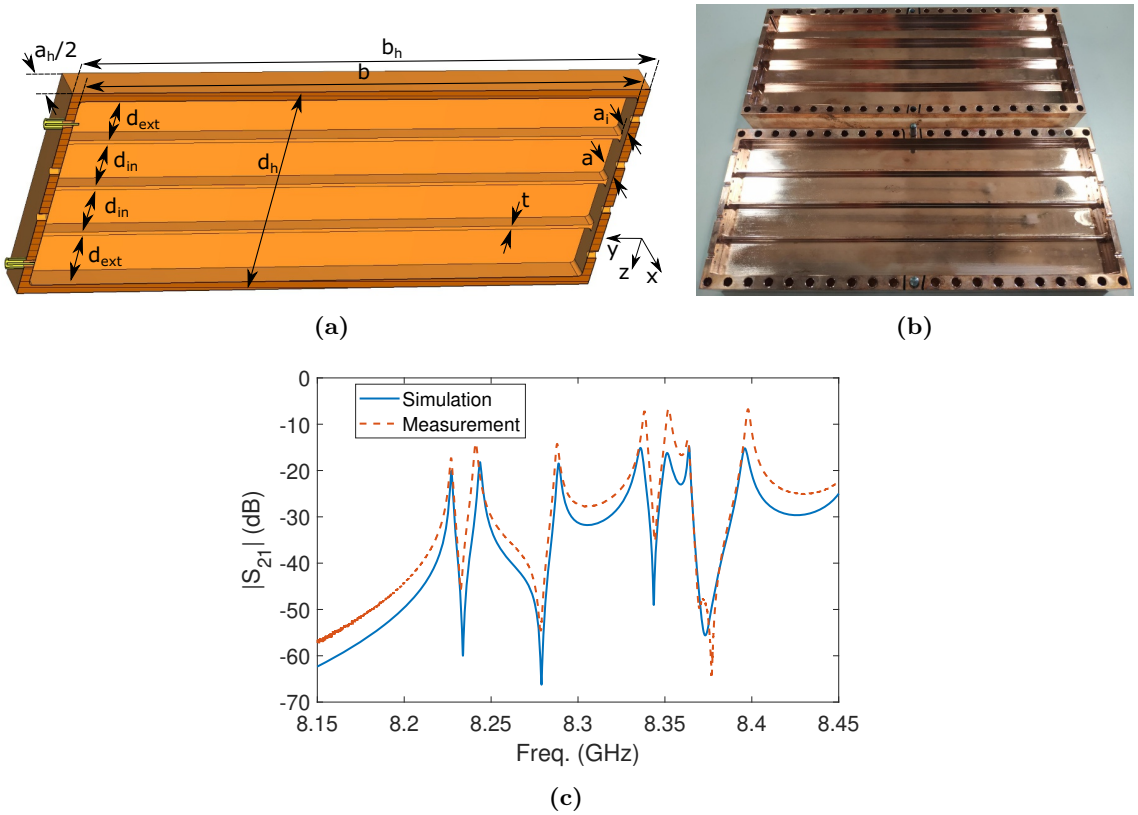

Figure 16. Manufactured haloscope prototype based on four tall subcavities with three inductive irises employing the in length coupling: (a) model of one of the two symmetrical halves, (b) picture of the manufactured structure divided in two symmetrical halves, and (c) S_{21} magnitude as a function of the frequency (simulation versus measurements at room temperature).

Freq. (GHz)	Resonant mode	Configuration
8.227	TE_{101}	[+ + + +]
8.241	TE_{111}	[+ + + +]
8.288	TE_{121}	[+ + + +]
8.338	TE_{101}	[+ + − −]
8.352	TE_{111}	[+ + − −]
8.363	TE_{131}	[+ + + +]
8.398	TE_{121}	[+ + − −]

Table 3. Description of the configuration and resonant modes that appear in figure 16c from measurements, and corresponding resonant frequencies.

Regarding the form factor, a value of $C = 0.625$ has been obtained, which can be further increased with an optimisation process. The configuration modes associated with the modes (resonances) that appear in the plot are enumerated in table 3.

The relative mode separation of this structure is $\Delta f = 0.17\%$ (14.3 MHz), which matches with figure 4a (right axis) for $b/a = 300/22.86 = 13.12$. The proximity of the next

JHEP08(2023)098

configuration mode ([+ + − −]) is not a problem because it is relatively far in frequency (1.35% or 111.4 MHz). The haloscope's overall volume is $V = 743\,\text{mL}$, and the total Q_0VC is $3.53 \times 10^4\,\text{L}$, which is 176 times that of a single normal WR-90 cavity.

Tall structures provide an additional benefit to alleviate the mode clustering issue: the presence of transmission zeros. They are created due to the interaction between cavity higher order modes when they are close in frequency. For example, a transmission zero appears at the right side of the axion mode (TE_{101}) due to the interaction between this mode and the TE_{111} resonance (phase cancellation between signals coupled to both modes [54]).

3.3 Large subcavities

A powerful strategy to increase the volume of a haloscope is to combine all the previous ideas: 1D multicavity concept with large (that is, long and tall) subcavities. Regarding the best stacking direction in large multicavities, it is expected to be very similar to that in long multicavities and tall multicavities. Considering only the mode separation limits and observing figures 10 and 15, it can be concluded that the coupling direction option with the best Q_0VC factor is the in height one with capacitive iris for both dipole and solenoid magnets. However, the best stacking direction option also depends on the magnet dimensions, taking into account the illustrations shown in figures 9 and 14.

For example, in the BabyIAXO dipole magnet, a long and tall multicavity structure stacked in width (similar to the cases from figures 9c and 14c but with long and tall subcavities) with $a = 17.85\,\text{mm}$, $b = \frac{\phi_{\text{BabyIAXO}}}{\sqrt{2}} - 2t_{Cu} = 414.26\,\text{mm}$, and $d = 1600\,\text{mm}$ (limited to avoid mode clustering issues, as depicts table 2) with $N = \lfloor \frac{b}{a+t} \rfloor = 20$ subcavities (where $t = 2\,\text{mm}$ is the thickness of the irises) could be implemented, which implies a volume of $V = 236.75\,\text{L}$. In the MRI (AMDX-EFR) solenoid magnet, a multicavity stacked in width (similar to the cases from figures 9f and 14f but with long and tall subcavities) with $a = 17.85\,\text{mm}$, $b = L_{\text{MRI}} = 513\,\text{mm}$, and $d = \frac{\phi_{\text{MRI}}}{\sqrt{2}} - 2t_{Cu} = 561.69\,\text{mm}$, with $N = \lfloor \frac{d}{a+t} \rfloor = 28$ subcavities could be implemented, providing a volume of $V = 144.24\,\text{L}$. Comparing the volume in both examples, the BabyIAXO case provides a greater value. However, despite the lower volume value (144.24 L versus 236.75 L) and observing equation (1.1), the lower system temperature (0.1 K versus 4.2 K) and the higher magnetic field (9 T versus 2.5 T) of the MRI (AMDX-EFR) magnet (see table 1) make this bore much more recommended between these two examples.

An all-inductive multicavity haloscope based on $N = 4$ large subcavities of $d = 100\,\text{mm}$ and $b = 100\,\text{mm}$ employing in width coupling has been designed as a preliminary proof of concept. Figure 17a shows the physical model of the haloscope. In this case, the selected physical coupling $|k|$ value and the resulting coupling matrix are those of the four tall subcavities design (see equation (3.4)) from the previous section. Figure 17b shows the simulation for the S_{21} magnitude as a function of the frequency. The dimensions of the structure are: length and height of all the subcavities $d = 100\,\text{mm}$ and $b = 100\,\text{mm}$, respectively; internal subcavities width $a_{\text{in}} = 17.6\,\text{mm}$; external subcavities width $a_{\text{ext}} = 17.85\,\text{mm}$; and width and thickness of all the inductive irises $a_i = 8.9\,\text{mm}$ and $t = 2\,\text{mm}$, respectively.

JHEP08(2023)098

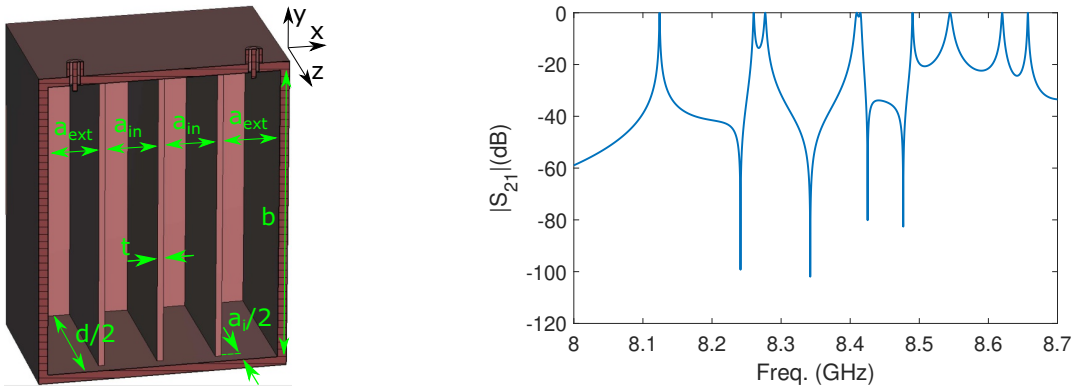

(a) (b)

Figure 17. All-inductive multicavity haloscope design based on four subcavities with three inductive irises combining the long and tall cavity concepts: (a) picture of a symmetrical half of the structure, and (b) simulated magnitude of S_{21} as a function of the frequency for $T = 2\,\mathrm{K}$.

Freq. (GHz)	Resonant mode	Configuration
8.124	TE_{101}	[+ + + +]
8.26	TE_{111}	[+ + + +]
8.277	TE_{101}	[+ + − −]
8.409	TE_{101}	[+ − − +]
8.415	TE_{111}	[+ + − −]
8.49	TE_{101}	[+ − + −]
8.544	TE_{111}	[+ − − +]
8.62	TE_{111}	[+ − + −]
8.657	TE_{121}	[+ + + +]

Table 4. List of the configuration and resonant modes shown in figure 17b, and corresponding resonant frequencies.

A quality and form factor value of $Q_0 = 58327$ (at $T = 2\,\mathrm{K}$) and $C = 0.464$, respectively, are obtained for the TE_{101} mode (the axion mode). The form factor for this structure was not optimised, and the mode localization effect should be examined (envisaged work is expected on this topic). The eigenmodes that appear in the plot are listed in table 4, with the axion mode being the one resonating at 8.124 GHz (the first resonance). The relative mode separation of this prototype is $\Delta f = 1.67\%$ (136 MHz). The position of the ports (at the centre of the subcavities) avoids the excitation of the TE_{102} resonance since this mode has a zero electric field at that position. Similarly to the previous structure (a tall multicavity with $N = 4$), the distance of the next configuration mode ([+ + − −]) is not a problem because it is far in frequency (1.88 % or 153 MHz) due to the low number of subcavities employed. In addition, analogously to the example of the previous section (tall structures), the response of this multicavity also shows transmission zeros produced

JHEP08(2023)098

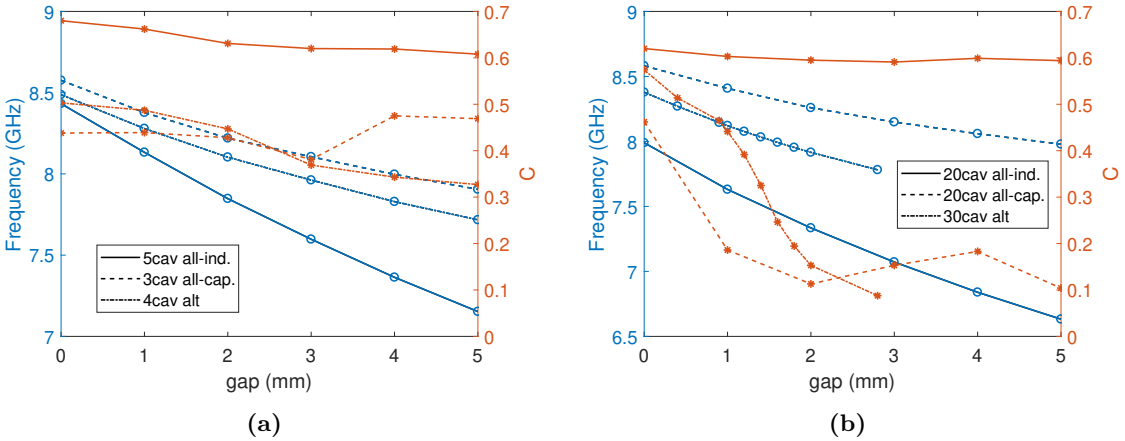

Figure 18. Frequency tuning (blue lines) and form factor (red lines) versus vertical cut opening gap for several multicavities: (a) 5cav all-inductive, 3cav all-capacitive, and 4cav alternated; and (b) 20cav all-inductive, 20cav all-capacitive, and 30cav alternated.

between resonant modes, aiding their separation when they are close in frequency. The volume of this haloscope is $V = 714\,\text{mL}$, resulting in $Q_0VC = 1.9 \times 10^4\,\text{L}$, which is ~ 96 times higher than a single standard WR-90 cavity.

3.4 Vertical cut tuning

Tuning simulations were carried out as a proof of concept in various 1D multicavities with conventional WR-90 subcavities stacked in length using the vertical cut technique [46] (see figure 6a). The main problem in this kind of structure when a vertical cut is applied is the form factor detriment due to mode localization when opening. For this reason, this work has been focused on analysing this parameter. Figure 18 shows the form factor variation for a gap between 0 and 5 mm for two types of multicavities: low number of subcavities ($N \leq 5$) and high number of subcavities ($N \geq 20$). As it can be observed, this parameter is decreased considerably for multicavities with high N when capacitive irises are employed (the all-capacitive and alternated scenarios). This behaviour occurs due to the high form factor sensitivity of these structures with their dimensions. On the other hand, mode separation and the quality factor give good results. Other tuning studies for 1D multicavities with large dimensions are reserved for a future line. The ferroelectric elements as an electronic tuning technique [47] are also being studied to solve the form factor issue.

4 2D and 3D multicavities

The 1D multicavities can be extended to 2D and 3D multicavities, which use interresonator coupling via irises to connect non-adjacent subcavities [52]. These structures can be folded horizontally or vertically, allowing an efficient fit inside the room of some magnet bores and providing transmission zeros for rejecting nearby modes. Figure 19 shows examples of 2D and 3D multicavity structures.

JHEP08(2023)098

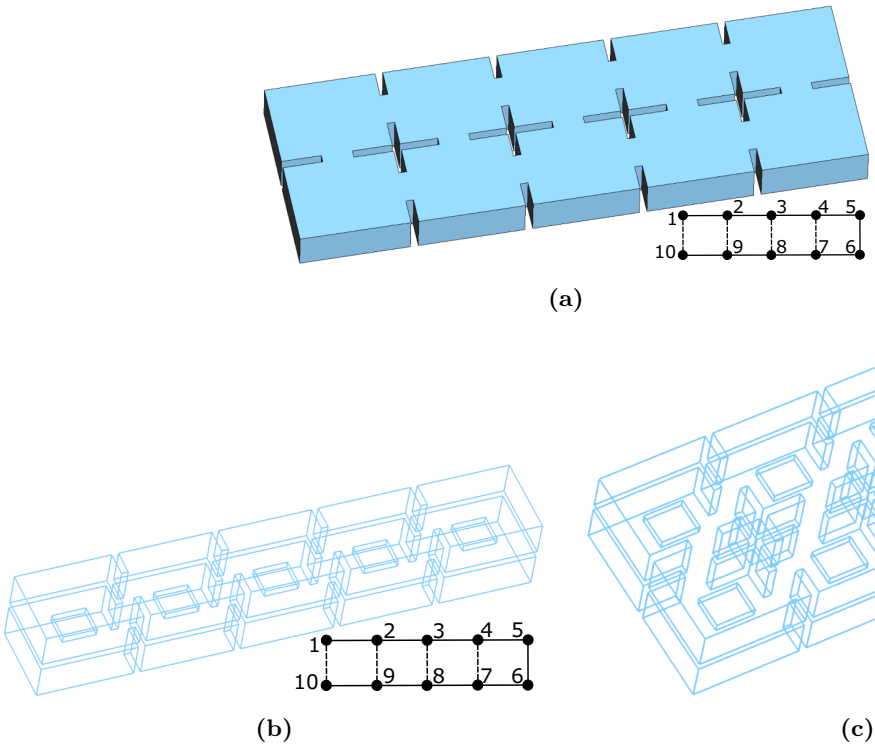

(a) (b) (c)

Figure 19. Examples of 2D and 3D structures with cross-couplings: (a) horizontally folded structure based on ten subcavities with four cross-couplings, (b) vertically folded structure with the same topology properties, and (c) 3D structure based on twelve subcavities with nine cross-couplings. A topology diagram is shown at the right-bottom corner of each case, where a solid line denotes the main coupling path while a dashed line indicates a cross-coupling.

The coupling matrices associated with the 2D and 3D examples shown in the topology diagrams from figure 19 are:

$$\mathbf{M_{2D}} = \begin{pmatrix} \Omega_1 & M_{1,2} & 0 & 0 & 0 & 0 & 0 & 0 & 0 & M_{1,10} \\ M_{1,2} & \Omega_2 & M_{2,3} & 0 & 0 & 0 & 0 & 0 & M_{2,9} & 0 \\ 0 & M_{2,3} & \Omega_3 & M_{3,4} & 0 & 0 & 0 & M_{3,8} & 0 & 0 \\ 0 & 0 & M_{3,4} & \Omega_4 & M_{4,5} & 0 & M_{4,7} & 0 & 0 & 0 \\ 0 & 0 & 0 & M_{4,5} & \Omega_5 & M_{5,6} & 0 & 0 & 0 & 0 \\ 0 & 0 & 0 & 0 & M_{5,6} & \Omega_6 & M_{6,7} & 0 & 0 & 0 \\ 0 & 0 & 0 & M_{4,7} & 0 & M_{6,7} & \Omega_7 & M_{7,8} & 0 & 0 \\ 0 & 0 & M_{3,8} & 0 & 0 & 0 & M_{7,8} & \Omega_8 & M_{8,9} & 0 \\ 0 & M_{2,9} & 0 & 0 & 0 & 0 & 0 & M_{8,9} & \Omega_9 & M_{9,10} \\ M_{1,10} & 0 & 0 & 0 & 0 & 0 & 0 & 0 & M_{9,10} & \Omega_{10} \end{pmatrix}, \tag{4.1}$$

$$\mathbf{M_{3D}} = \begin{pmatrix} \Omega_1 & M_{1,2} & 0 & 0 & 0 & M_{1,6} & 0 & 0 & 0 & 0 & 0 & M_{1,12} \\ M_{1,2} & \Omega_2 & M_{2,3} & 0 & M_{2,5} & 0 & 0 & 0 & 0 & 0 & M_{2,11} & 0 \\ 0 & M_{2,3} & \Omega_3 & M_{3,4} & 0 & 0 & 0 & 0 & 0 & M_{3,10} & 0 & 0 \\ 0 & 0 & M_{3,4} & \Omega_4 & M_{4,5} & 0 & 0 & 0 & M_{4,9} & 0 & 0 & 0 \\ 0 & M_{2,5} & 0 & M_{4,5} & \Omega_5 & M_{5,6} & 0 & M_{5,8} & 0 & 0 & 0 & 0 \\ M_{1,6} & 0 & 0 & 0 & M_{5,6} & \Omega_6 & M_{6,7} & 0 & 0 & 0 & 0 & 0 \\ 0 & 0 & 0 & 0 & 0 & M_{6,7} & \Omega_7 & M_{7,8} & 0 & 0 & 0 & M_{7,12} \\ 0 & 0 & 0 & 0 & M_{5,8} & 0 & M_{7,8} & \Omega_8 & M_{8,9} & 0 & M_{8,11} & 0 \\ 0 & 0 & 0 & M_{4,9} & 0 & 0 & 0 & M_{8,9} & \Omega_9 & M_{9,10} & 0 & 0 \\ 0 & 0 & M_{3,10} & 0 & 0 & 0 & 0 & 0 & M_{9,10} & \Omega_{10} & M_{10,11} & 0 \\ 0 & M_{2,11} & 0 & 0 & 0 & 0 & 0 & M_{8,11} & 0 & M_{10,11} & \Omega_{11} & M_{11,12} \\ M_{1,12} & 0 & 0 & 0 & 0 & 0 & M_{7,12} & 0 & 0 & 0 & M_{11,12} & \Omega_{12} \end{pmatrix}. \tag{4.2}$$

JHEP08(2023)098

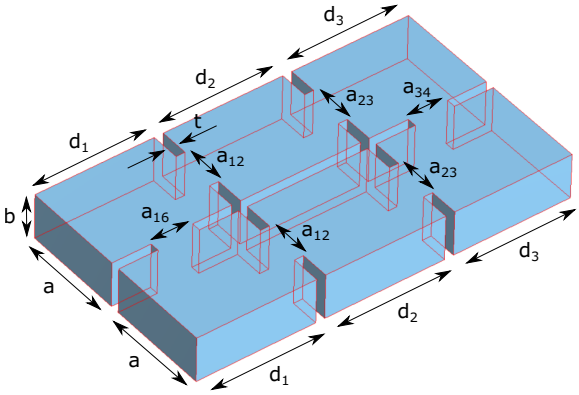

Figure 20. Model of a 6 subcavities 2D multicavity horizontally folded (two symmetrical rows with three subcavities per row). It is based on an all-inductive coupled multicavity structure. An inductive iris between the 1^{st} and 6^{th} subcavity is introduced thanks to the physical folding applied in the horizontal plane.

The three main diagonals of both matrices have the same behaviour as in equation (3.1). However, for 2D and 3D topologies, an anti-diagonal with a non-zero value appears due to the new cross-couplings. In addition, for 3D structures, other cross-couplings can appear due to the folding introduced in the two axes (horizontal and vertical), as depicted in the model shown in figure 19c. This is the case of the elements $M_{1,6}$, $M_{2,5}$, $M_{7,12}$, and $M_{8,11}$ (and their symmetrical pairs).

As a first proof of concept, a rigorous study has been carried out in which different types of topologies have been tested on an all-inductive 2D multicavity structure. The study was conducted on $N = 6$ subcavities folded horizontally (three subcavities per row), each with standard dimensions. The main objective of this study is to find a topology that rejects the next eigenmode to the axion one in order to improve the mode clustering issue. This has been achieved with only one cross-coupling, just placing a window iris between the first and last (6^{th}) subcavities. This prototype has been designed, optimised, and manufactured.

In the design of this structure, the following coupling matrix has been employed for the development of the geometry parameters:

$$\mathbf{M} = \begin{pmatrix} 1 & -0.5 & 0 & 0 & 0 & -0.5 \\ -0.5 & 1 & -0.5 & 0 & 0 & 0 \\ 0 & -0.5 & 1 & -0.5 & 0 & 0 \\ 0 & 0 & -0.5 & 1 & -0.5 & 0 \\ 0 & 0 & 0 & -0.5 & 1 & -0.5 \\ -0.5 & 0 & 0 & 0 & -0.5 & 1 \end{pmatrix}. \tag{4.3}$$

As can be seen in equation (4.3), a non zero value is selected for the elements M_{16} and M_{61} due to the use of a cross-coupling iris. From this coupling matrix, it can be observed that the sign for all the interresonator couplings is negative ($k < 0$). This indicates that the structure can be implemented with all irises of the inductive type (even the cross-coupling one). The model of this structure is shown in figure 20.

Two pictures of the fabricated prototype are shown in figures 21a and 21b. The optimisation process has been based on adjusting the frequency position of one of the transmission zeros to cancel the closest mode. This cancellation of the closest mode can be

JHEP08(2023)098

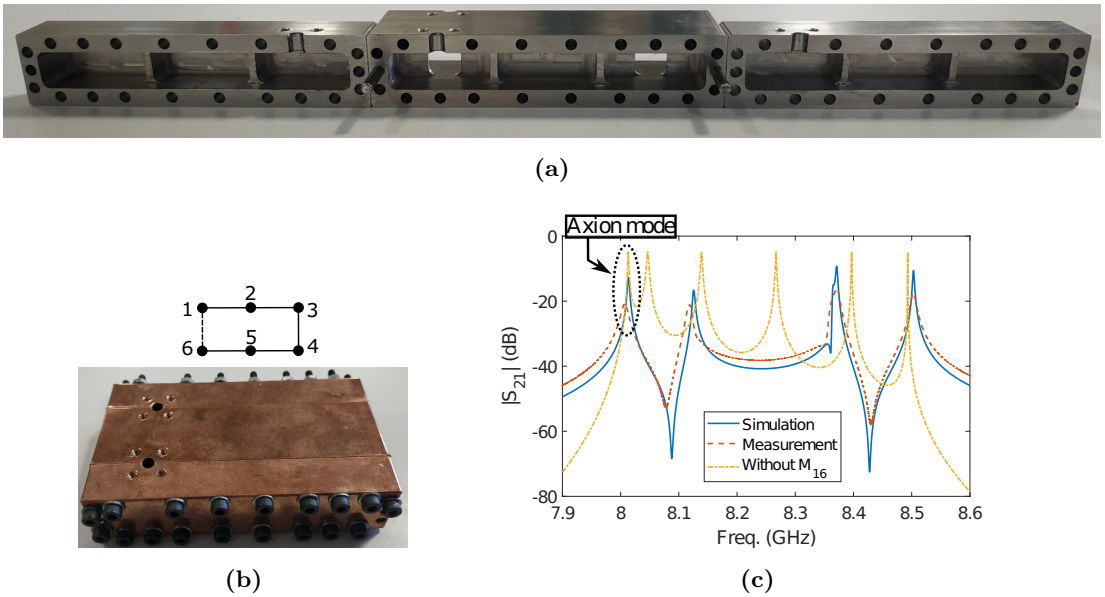

Figure 21. Structure based on six subcavities with a cross-coupling between the first and the last subcavities: (a) picture of the manufactured pieces (three parts), (b) topology diagram and copper coated final structure already mounted, and (c) S_{21} magnitude as a function of the frequency (simulation versus measurements at room temperature). The analytical response of a 1D 6-subcavities structure has been added to show the cancellation of the closest mode due to one transmission zero.

observed in figure 21c, which plots the S_{21} magnitude as a function of the frequency for the optimised design in comparison with experimental results and with the response of a 1D multicavity based on 6 subcavities. The final dimensions of this structure (see figure 20) are: $a = 22.86\,\text{mm}$, $b = 10.16\,\text{mm}$, $d_1 = 26.516\,\text{mm}$, $d_2 = 26.845\,\text{mm}$, $d_3 = 26.503\,\text{mm}$, $a_{12} = a_{23} = 9.921\,\text{mm}$, $a_{34} = 8.894\,\text{mm}$, $a_{16} = 9.203\,\text{mm}$, and thickness of all the inductive irises $t = 2\,\text{mm}$.

As it is shown in figure 21c, the mode separation from the axion mode (obtained at 8.013 GHz) to the next eigenmode is $\Delta f = 1.58\%$ (127 MHz) in simulation and $\Delta f = 1.39\%$ (111 MHz) in measurements (without cross-coupling it is $\Delta f = 0.42\%$ (34 MHz)). A good agreement is observed between simulation results and measurements. From simulations employing copper material, a $Q_0^{2K} = 40000$ is predicted for the axion mode at cryogenic temperatures and $Q_0^{300K} = 6800$ at room temperature. The measurements from the manufactured structure at room temperature provide a value of $Q_0 = 4000$ with the copper coated structure, which is 60% of the simulation result. The obtained form factor for this mode is $C = 0.702$. Note how, for this multicavity structure, a form factor higher than the theoretical one for a single cavity is obtained. This occurs due to the use of several subcavities connected by irises, in which one of the configuration modes is cancelled by one transmission zero. Therefore, these transmission zeros provide a good avenue not only for improving mode clustering but also for slightly increasing the form factor. Even higher performances could be achieved when 2D and 3D geometries are combined with long, tall,

JHEP08(2023)098

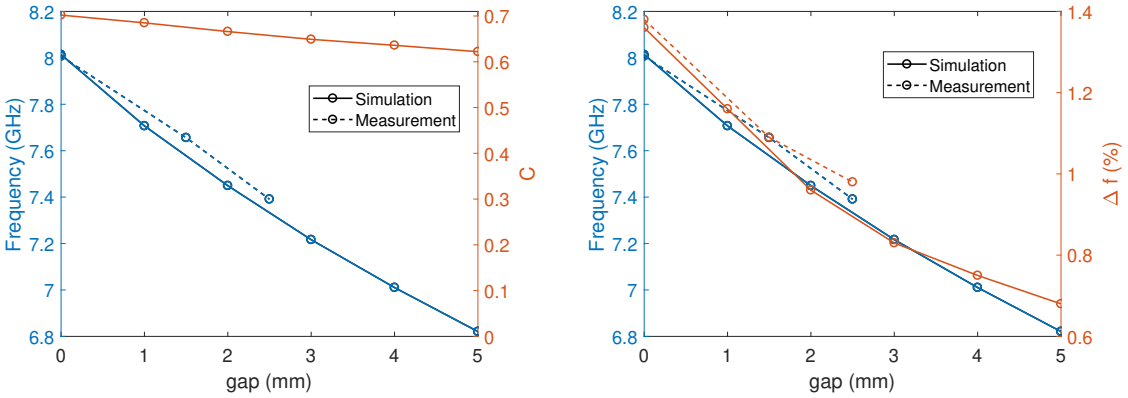

Figure 22. (a) Frequency tuning (blue lines) and form factor (red lines), and (b) frequency tuning (blue lines) and mode separation (red lines), versus vertical cut opening gap for the 2D multicavity design from figure 21. Simulation (solid lines) and measurement (dashed lines) results are included.

or large subcavities (and with the alternating coupling concept) regarding the main topics covered for multicavities in this work, that is, the Q_0VC factor, the mode clustering (Δf), the realisable interresonator physical coupling (k), the use of transmission zeros by cross-coupling, and the bore sizes in dipole and solenoid magnets.

In the case of this prototype, the total volume obtained is $V = 38\,\text{mL}$, and $Q_0VC = 1067\,\text{L}$, which is 5.33 times higher than that obtained by a single standard WR-90 cavity.

In addition, tuning studies were conducted to check the form factor and mode separation behaviour in this design employing the vertical cut technique [46] (see figure 6a). In this case, a synchronous displacement of the lateral parts (fixing the position of the central piece) has been carried out for this tuning with the two vertical cuts employed for the manufacture of the prototype (see figures 21a and 21b). Figure 22a shows the frequency tuning range obtained and the form factor detriment for a gap between 0 and 5 mm. For the frequency shift, measurement results have been included for a gap between 0 and 2.5 mm. On the other hand, figure 22b shows the mode separation reduction (due to the separation from the optimal point, at $gap = 0$) for a gap between 0 and 5 mm. Also, measurement results are added for a gap between 0 and 2.5 mm for this parameter. For both frequency tuning and mode separation parameters, simulation and measurement results are in good agreement.

Since the obtained form factor is quite high for all gap cases ($C \in [0.62, 0.7]$), the whole studied range can be used, and it can be stated that a significantly high frequency tuning range has been achieved (1.19 GHz (16.1%)). As for the mode separation, although there has been a detriment of up to $\Delta f = 0.68\%$ for the $gap = 5\,\text{mm}$ case, this is still better than in the case of a six subcavities multicavity without cross-coupling ($\Delta f = 0.42\%$). The high decrease in mode separation when opening the vertical cuts comes from the sensitivity of the transmission zero (which rejects the closest configuration mode) to the

JHEP08(2023)098

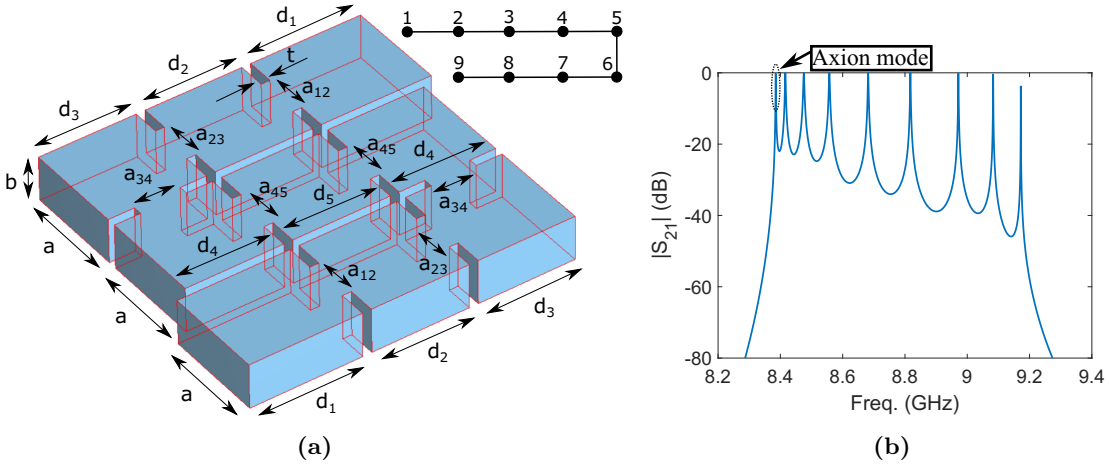

(a) **(b)**

Figure 23. Structure based on nine subcavities with a meander shape (2D geometry): (a) picture of the model, (b) simulated S_{21} magnitude as a function of the frequency. The topology diagram is shown in the right-top corner of (a).

structure dimensions. In addition, the quality factor gives good results for this range of gaps. Other tuning studies for 2D multicavities with more complex topologies are reserved for a future line.

As a final study of this work, an interesting 2D geometry is now proposed to more efficiently use the available magnet bore footprint. The design is simpler than the previous one since it has no cross-couplings (and therefore no transmission zeros). The idea is based on introducing a meandering multicavity geometry, as shown in figure 23a. Also, in figure 23b, the S_{21} magnitude as a function of the frequency is shown. The axion mode is the first resonance in the response since the structure is based on all inductive irises.

Although the geometry of this structure is 2D topologically it is 1D, since it implements only couplings from adjacent resonators. This can be observed in its coupling matrix:

$$\mathbf{M} = \begin{pmatrix} 0.5 & -0.5 & 0 & 0 & 0 & 0 & 0 & 0 & 0 \\ -0.5 & 1 & -0.5 & 0 & 0 & 0 & 0 & 0 & 0 \\ 0 & -0.5 & 1 & -0.5 & 0 & 0 & 0 & 0 & 0 \\ 0 & 0 & -0.5 & 1 & -0.5 & 0 & 0 & 0 & 0 \\ 0 & 0 & 0 & -0.5 & 1 & -0.5 & 0 & 0 & 0 \\ 0 & 0 & 0 & 0 & -0.5 & 1 & -0.5 & 0 & 0 \\ 0 & 0 & 0 & 0 & 0 & -0.5 & 1 & -0.5 & 0 \\ 0 & 0 & 0 & 0 & 0 & 0 & -0.5 & 1 & -0.5 \\ 0 & 0 & 0 & 0 & 0 & 0 & 0 & -0.5 & 0.5 \end{pmatrix}. \tag{4.4}$$

The final dimensions of this structure (see figure 23a) are: $a = 22.86\,\text{mm}$, $b = 10.16\,\text{mm}$, $d_1 = 25.2\,\text{mm}$, $d_2 = d_3 = d_4 = d_5 = 22\,\text{mm}$, and width and thickness of all the inductive irises $a_{12} = a_{23} = a_{34} = a_{45} = 10.25\,\text{mm}$ and $t = 2\,\text{mm}$, respectively. This design provides an axion mode frequency of $f_a = 8.385\,\text{GHz}$, and a form and quality factor of $C = 0.684$ and $Q_0^{2K} = 41475$, respectively, which corresponds with very good results compared to previous designs from RADES and the ones shown in this work. The mode clustering value Δf is 0.37% (30.8 MHz), in accordance with the results from figure 8b. The resulting total volume of the haloscope is $V = 49.14\,\text{mL}$, and the total Q_0VC is 1394.05 L, which is 6.96 times that of a single standard WR-90 cavity.

JHEP08(2023)098

The benefits of this haloscope geometry are based on its quasi-square shape. In this case, the detector provides a footprint of $72.58 \times 76.4\,\mathrm{mm}^2$ (along width and length), while in a 1D geometry, these nine subcavities give an elongated shape of $22.86 \times 286.4\,\mathrm{mm}^2$. This quasi-square area may be more appropriate in some cases where the magnet bore is limited in all dimensions (as it occurs with some solenoid magnets; see, for instance, figure 9f). In practise, some of the ideas proposed in this paper can be combined to use more efficiently the available space in magnet bores extensively used by the axion search community.

5 Conclusions and prospects

In this work, the volume limits of rectangular haloscopes have been explored. The increase of this parameter improves the Q_0VC figure of merit and, ultimately, the axion detection sensitivity $g_{a\gamma}$. Different strategies for increasing the volume, taking into account certain constraints such as the frequency separation between adjacent modes (mode clustering) and the variation of the form and quality factors, are presented. Also, exhaustive studies with single cavities and 1D multicavities and, in a more introductory way, 2D and 3D multicavities achieving large Q_0VC factors, are shown. The compatibility of these haloscopes with the largest dipole and solenoid magnets in the axion community has been demonstrated. Several practical designs have been manufactured and measured, providing good results in quality factor, form factor, and mode clustering, illustrating the capabilities of some of these studies while serving as validation.

It has been found that among single cavities, large cavities provide the best Q_0VC performance. In addition, it has also been shown that, despite their greater complexity in the design process, the use of multicavities can lead to an improvement in this factor. Nevertheless, when searching the axion for a range of masses, the increase in volume is limited by the number of mode crossings that can be tolerated. In 1D multicavities, all-capacitive structures with subcavities stacked in height give the best results in Q_0VC factor. On the other hand, novel results have been obtained in this paper where the appearance of transmission zeros in some multicavity designs allows to shift or suppress modes close to the axion one, thus reducing both the mode clustering at one frequency and the possible mode crossings in a range of frequencies. These techniques are intended to serve as a manual for any experimental axion group wishing to search for volume limits in the design of a haloscope based on rectangular cavities to be placed inside both dipole or solenoid magnets. Nevertheless, these strategies and analyses are also useful for any application where increasing the volume of the device at a given frequency is a goal.

On the other hand, preliminary tuning investigations have been conducted employing the vertical cut technique for several single and multicavity (1D and 2D) cases. The results reveal a competitive performance for long cavities. For multicavities, the form factor suffers from high instability when capacitive irises are used. More research is being carried out along these lines to avoid these issues, such as the use of ferroelectric materials.

A wide range of promising possibilities opens up from this analysis, depending on the type and configuration of the data taking magnet. The strategies described in this work allow for the best use of the bore space with the aim of optimising the sensitivity of axion

JHEP08(2023)098

search experiments. In this regard, the study of the rectangular geometry limits employing several ideas proposed in this work, such as the alternating coupling in 1D multicavities or the long, tall, and large subcavities in 2D/3D multicavities, is a recommendable task for the design of a high competitive haloscope in the axion community. Finally, similar analyses and tests will be investigated for cylindrical haloscopes in future work.

Acknowledgments

This work was performed within the RADES group. We thank our colleagues for their support. In addition, this work has been funded by the grant PID2019-108122GB-C33, funded by MCIN/AEI/10.13039/501100011033/ and by "ERDF A way of making Europe". JMGB thanks the grant FPI BES-2017-079787, funded by MCIN/AEI/10.13039/501100011033 and by "ESF Investing in your future". Also, this project has received partial funding through the European Research Council under grant ERC-2018-StG-802836 (AxScale).

References

[1] R.D. Peccei and H.R. Quinn, *CP Conservation in the Presence of Instantons*, *Phys. Rev. Lett.* **38** (1977) 1440 [INSPIRE].

[2] R.D. Peccei and H.R. Quinn, *Constraints imposed by CP conservation in the presence of instantons*, *Phys. Rev. D* **16** (1977) 1791 [INSPIRE].

[3] S. Weinberg, *A new light boson?*, *Phys. Rev. Lett.* **40** (1978) 223 [INSPIRE].

[4] F. Wilczek, *Problem of strong P and T invariance in the presence of instantons*, *Phys. Rev. Lett.* **40** (1978) 279 [INSPIRE].

[5] J. Preskill, M.B. Wise and F. Wilczek, *Cosmology of the invisible axion*, *Phys. Lett. B* **120** (1983) 127 [INSPIRE].

[6] L.F. Abbott and P. Sikivie, *A cosmological bound on the invisible axion*, *Phys. Lett. B* **120** (1983) 133 [INSPIRE].

[7] M. Dine and W. Fischler, *The not-so-harmless axion*, *Phys. Lett. B* **120** (1983) 137 [INSPIRE].

[8] I.G. Irastorza and J. Redondo, *New experimental approaches in the search for axion-like particles*, *Prog. Part. Nucl. Phys.* **102** (2018) 89 [arXiv:1801.08127] [INSPIRE].

[9] H. Primakoff, *Photoproduction of neutral mesons in nuclear electric fields and the mean life of the neutral meson*, *Phys. Rev.* **81** (1951) 899 [INSPIRE].

[10] P. Sikivie, *Experimental tests of the invisible axion*, *Phys. Rev. Lett.* **51** (1983) 1415 [*Erratum ibid.* **52** (1984) 695] [INSPIRE].

[11] I. Stern, *ADMX status*, *PoS* **ICHEP2016** (2016) 198 [arXiv:1612.08296] [INSPIRE].

JHEP08(2023)098

[12] A.K. Yi et al., *Axion Dark Matter Search around 4.55 μeV with Dine-Fischler-Srednicki-Zhitnitskii Sensitivity*, *Phys. Rev. Lett.* **130** (2023) 071002 [arXiv:2210.10961] [INSPIRE].

[13] CAST collaboration, *New CAST Limit on the Axion-Photon Interaction*, *Nature Phys.* **13** (2017) 584 [arXiv:1705.02290] [INSPIRE].

[14] E. Armengaud et al., *Conceptual design of the international axion observatory (IAXO)*, 2014 *JINST* **9** T05002 [arXiv:1401.3233] [INSPIRE].

[15] IAXO collaboration, *Conceptual design of BabyIAXO, the intermediate stage towards the International Axion Observatory*, *JHEP* **05** (2021) 137 [arXiv:2010.12076] [INSPIRE].

[16] ADMX collaboration, *Extended Search for the Invisible Axion with the Axion Dark Matter Experiment*, *Phys. Rev. Lett.* **124** (2020) 101303 [arXiv:1910.08638] [INSPIRE].

[17] HAYSTAC collaboration, *A quantum-enhanced search for dark matter axions*, *Nature* **590** (2021) 238 [arXiv:2008.01853] [INSPIRE].

[18] HAYSTAC collaboration, *Results from phase 1 of the HAYSTAC microwave cavity axion experiment*, *Phys. Rev. D* **97** (2018) 092001 [arXiv:1803.03690] [INSPIRE].

[19] CAST collaboration, *First results of the CAST-RADES haloscope search for axions at 34.67 μeV*, *JHEP* **21** (2020) 075 [arXiv:2104.13798] [INSPIRE].

[20] D. Alesini et al., *Search for galactic axions with a high-q dielectric cavity*, *Phys. Rev. D* **106** (2022) 052007 [arXiv:2208.12670] [INSPIRE].

[21] D. Alesini, D. Babusci, D. Di Gioacchino, C. Gatti, G. Lamanna and C. Ligi, *The KLASH Proposal*, arXiv:1707.06010 [INSPIRE].

[22] A. Díaz-Morcillo et al., *Design of new resonant haloscopes in the search for the dark matter axion: A review of the first steps in the RADES collaboration*, *Universe* **8** (2021) 5 [arXiv:2111.14510] [INSPIRE].

[23] D. Kim, J. Jeong, S. Youn, Y. Kim and Y.K. Semertzidis, *Revisiting the detection rate for axion haloscopes*, *JCAP* **03** (2020) 066 [arXiv:2001.05605] [INSPIRE].

[24] B.M. Brubaker, *First results from the HAYSTAC axion search*, Ph.D. Thesis, Yale University, New Haven, U.S.A. (2017) [arXiv:1801.00835] [INSPIRE].

[25] C.M. Adair et al., *Search for Dark Matter Axions with CAST-CAPP*, *Nature Commun.* **13** (2022) 6180 [arXiv:2211.02902] [INSPIRE].

[26] K. Zioutas et al., *A decommissioned LHC model magnet as an axion telescope*, *Nucl. Instrum. Meth. A* **425** (1999) 480 [astro-ph/9801176] [INSPIRE].

[27] J. Golm et al., *Thin film (high temperature) superconducting radiofrequency cavities for the search of axion dark matter*, *IEEE Trans. Appl. Supercond.* **32** (2022) 1500605 [arXiv:2110.01296] [INSPIRE].

[28] C. Bartram, *Venturing a glimpse of the dark matter halo with ADMX*, talk in *Cambridge Workshop on Axion Physics*, Cambridge, U.S.A. (2021).

[29] G. Carosi, *Axion Detection Experiments*, talk in *PPC 2022: XV International Conference on Interconnections between Particle Physics & Cosmology*, St. Louis, U.S.A. (2022).

[30] G. Carosi and K. Van Bibber, *Status of the ADMX and ADMX-HF experiments*, talk in *8th Patras Workshop on Axions, WIMPs, and WISPs*, Chicago, U.S.A. (2012), https://www.osti.gov/biblio/1078551.

JHEP08(2023)098

[31] R. Battesti et al., *High magnetic fields for fundamental physics*, *Phys. Rept.* **765-766** (2018) 1 [arXiv:1803.07547] [INSPIRE].

[32] W. Ma et al., *A new member of high field large bore superconducting research magnets family*, *IOP Conf. Ser. Mater. Sci. Eng.* **502** (2019) 012104.

[33] M. Simanovskaia and K. van Bibber, *Status of the ADMX-HF Experiment*, in *11th Patras Workshop on Axions, WIMPs and WISPs*, Zaragoza, Spain (2015), pg. 157, https://doi.org/10.3204/DESY-PROC-2015-02/simanovskaia_maria [INSPIRE].

[34] J. Choi, S. Ahn, B.R. Ko, S. Lee and Y.K. Semertzidis, *CAPP-8TB: Axion dark matter search experiment around* 6.7 μev, *Nucl. Instrum. Meth. A* **1013** (2021) 165667 [arXiv:2007.07468] [INSPIRE].

[35] B.T. McAllister et al., *The ORGAN Experiment: An axion haloscope above 15 GHz*, *Phys. Dark Univ.* **18** (2017) 67 [arXiv:1706.00209] [INSPIRE].

[36] G. Carosi, G. Rybka and K. van Bibber eds., *Proceedings of 2nd Workshop on Microwave Cavities and Detectors for Axion Research*, Livermore, U.S.A. (2017) [*Springer Proc. Phys.* **211** (2018) 1 [INSPIRE].

[37] Y. Lee et al., *Searching for Invisible Axion Dark Matter with an 18 T Magnet Haloscope*, *Phys. Rev. Lett.* **128** (2022) 241805 [arXiv:2206.08845] [INSPIRE].

[38] H. Yoon et al., *Axion haloscope using an 18 T high temperature superconducting magnet*, *Phys. Rev. D* **106** (2022) 092007 [arXiv:2206.12271] [INSPIRE].

[39] B. Aja et al., *The Canfranc Axion Detection Experiment (CADEx): search for axions at 90 GHz with Kinetic Inductance Detectors*, *JCAP* **11** (2022) 044 [arXiv:2206.02980] [INSPIRE].

[40] CADEx collaboration, *Expression of Interest to the Laboratorio Subterráneo de Canfranc (LSC) - The Canfranc Axion Detection Experiment (CADEx)*, talk in *29th LSC SC meeting*, Virtual Meeting Online (2021).

[41] N. Crescini, *Towards the development of the ferromagnetic axion haloscope*, Ph.D. Thesis, University of Padua, Padua, Italy (2019), https://www.research.unipd.it/handle/11577/3425918.

[42] B.R. Ko et al., *Electric and magnetic energy at axion haloscopes*, *Phys. Rev. D* **94** (2016) 111702 [arXiv:1608.00843] [INSPIRE].

[43] J. Choi, H. Themann, M.J. Lee, B.R. Ko and Y.K. Semertzidis, *First axion dark matter search with toroidal geometry*, *Phys. Rev. D* **96** (2017) 061102 [arXiv:1704.07957] [INSPIRE].

[44] C.A. Balanis, *Advanced Engineering Electromagnetics*, John Wiley & Sons (1989).

[45] C. Ramella, M. Pirola and S. Corbellini, *Accurate characterization of high-Q microwave resonances for metrology applications*, *IEEE J. Microw.* **1** (2021) 610.

[46] S. Arguedas Cuendis et al., *The 3 Cavity Prototypes of RADES: An Axion Detector Using Microwave Filters at CAST*, *Springer Proc. Phys.* **245** (2020) 45 [arXiv:1903.04323] [INSPIRE].

[47] J.M. García-Barceló et al., *On the development of new tuning and inter-coupling techniques using ferroelectric materials in the detection of dark matter axions*, *IEEE Access* **11** (2023) 30360.

JHEP08(2023)098

[48] J. Jeong et al., *Search for Invisible Axion Dark Matter with a Multiple-Cell Haloscope*, *Phys. Rev. Lett.* **125** (2020) 221302 [arXiv:2008.10141] [INSPIRE].

[49] J. Jeong, S. Youn and J.E. Kim, *Multiple-cell cavity design for high mass axion searches: An extended study*, *Nucl. Instrum. Meth. A* **1053** (2023) 168327 [arXiv:2205.01319] [INSPIRE].

[50] A.A. Melcón et al., *Axion Searches with Microwave Filters: the RADES project*, *JCAP* **05** (2018) 040 [arXiv:1803.01243] [INSPIRE].

[51] A. Álvarez Melcón et al., *Scalable haloscopes for axion dark matter detection in the 30 μeV range with RADES*, *JHEP* **07** (2020) 084 [arXiv:2002.07639] [INSPIRE].

[52] R.J. Cameron, C.M. Kudsia and R.R. Mansour, *Microwave filters for communication systems: fundamentals, design, and applications*, second edition, Wiley (2018).

[53] https://www.3ds.com/products-services/simulia/products/cst-studio-suite/.

[54] M. Guglielmi, F. Montauti, L. Pellegrini and P. Arcioni, *Implementing transmission zeros in inductive-window bandpass filters*, *IEEE Trans. Microw. Theory Tech.* **43** (1995) 1911.

JHEP08(2023)098